Title

Attosecond response of molecules to impulsive ionization

Journal

NATURE PHYSICS

ISSN

1745-2473

Authors

Driver, Taran

Guo, Zhaoheng

Isele, Erik

et al.

Publication Date

2026-07-20

DOI

10.1038/s41567-026-03360-x

Peer reviewed

Attosecond Molecular Response to Impulsive Ionization

Taran Driver*†[1,2], Zhaoheng Guo*[3,4], Erik Isele*[1,2,3], Gilbert Grell*[5,6], Marco Ruberti*[7], Jordan T. O'Neal[1,2,8], Oliver Alexander[7], Sandra Beauvarlet[9,1], David Cesar[4], Joseph Duris[4], Douglas Garratt[1,2], Kirk A. Larsen[1,2], Siqi Li[4], Přemysl Kolorenč[10], Gregory A. McCracken[11], Daniel Tuthill[11], Zifan Wang[11], Nora Berrah[9], Christoph Bostedt[12,13], Kurtis Borne[2,14], Xinxin Cheng[2], Louis F. DiMauro[11], Gilles Doumy[15], Paris L. Franz[3,4], Andrei Kamalov[2], Xiang Li[2], Ming-Fu Lin[2], Razib Obaid[2], Antonio Pícon[6], River R. Robles[3,4], Daniel Rolles[14], Artem Rudenko[14], Moniruzzaman Shaikh[16], Daniel S. Slaughter[16], Nicholas S. Sudar[4], Emily Thierstein[1,2,3], Kiyoshi Ueda[17], Enliang Wang[14], Anna L. Wang[1,2,3], Thorsten Weber[16], Thomas J. A. Wolf[1,2], Linda Young[15,18], Zhen Zhang[4], Vitali Averbukh[7], Oliver Gessner[16], Philip H. Bucksbaum[1,3,8], Matthias F. Kling[2,19], Alicia Palacios[6], Fernando Martín‡[6], Jon P. Marangos§[7], Peter Walter[2], Agostino Marinelli¶[2,4,19], and James P. Cryan‖[1,2]

[1]*Stanford PULSE Institute, SLAC National Accelerator Laboratory, Menlo Park, CA, USA*

[2]*Linac Coherent Light Source, SLAC National Accelerator Laboratory, Menlo Park, CA, USA*

[3]*Department of Applied Physics, Stanford University, Stanford, CA, USA*

[4]*SLAC National Accelerator Laboratory, Menlo Park, CA, USA*

[5]*Instituto Madrileño de Estudios Avanzados en Nanociencia (IMDEA-Nanociencia), Madrid, Spain*

[6]*Departamento de Química, Universidad Autónoma de Madrid, Madrid, Spain*

[7]*The Blackett Laboratory, Imperial College London, London, United Kingdom*

[8]*Department of Physics, Stanford University, Stanford, CA, USA*

[9]*Department of Physics, University of Connecticut, Storrs, Connecticut, USA*

[10]*Faculty of Mathematics and Physics, Institute of Theoretical Physics, Charles University, Prague, Czechia*

[11]*Department of Physics, The Ohio State University, Columbus, Ohio, USA*

[12]*Paul Scherrer Institute, Villigen, Switzerland*

[13]*LUXS Laboratory for Ultrafast X-ray Sciences, Institute of Chemical Sciences and Engineering, Ecole Polytechnique Federale de Lausanne (EPFL), Lausanne, Switzerland*

[14]*J.R. Macdonald Laboratory, Kansas State University, Manhattan, Kansas, USA*

[15]*Chemical Sciences and Engineering Division, Argonne National Laboratory, Lemont, IL, USA*

[16]*Chemical Sciences Division, Lawerence Berkeley National Laboratory, Berkeley, California, USA*

[17]*Department of Chemistry, Tohoku University, Sendai, Japan*

[18]*Department of Physics and James Franck Institute, The University of Chicago, Chicago, IL, USA*

[19]*Department of Photon Science, SLAC National Accelerator Laboratory, Menlo Park, CA, USA*

Abstract

When matter interacts with energetic radiation it can undergo sudden, or *impulsive*, ionization. Impulsive ionization can drive important processes in chemistry and can be induced by cosmic rays and short-wavelength light, so it is ubiquitous in space and planetary atmospheres. A comprehensive understanding of this process lies at the limits of our current theoretical and computational capabilities. A full treatment requires advanced theoretical descriptions of electron correlation and complex nonadiabatic dynamics beyond the Born-Oppenheimer approximation. New experimental results are required to validate existing models. In this work we measure the response of the para-aminophenol molecule to sudden ionization. Using attosecond X-ray absorption spectroscopy, we resolve the ultrafast dynamics of the ionized molecule with atomic precision. A sub-femtosecond decay is assigned to states undergoing nonradiative decay, while few-femtosecond oscillatory signatures are associated with electronic wavepacket motion in stable cation states that will eventually couple to nuclear motion. We compare our measurement with state-of-the-art computational modeling, qualitatively reproducing the observed response across multiple timescales. Our work provides a vital benchmark for computational models of sudden ionization and ultrafast charge motion in matter.

*Authors Contributed Equally
†tdriver@stanford.edu
‡fernando.martin@uam.es
§j.marangos@imperial.ac.uk
¶marinelli@slac.stanford.edu
‖jcryan@slac.stanford.edu

Main

The motion of electrons plays a fundamental role in scientific and technological applications, ranging from the earliest stages of chemical reactions [1] to solar energy harvesting [2], light-driven catalysis [3] and next-generation microelectronics [4, 5]. The importance of electronic motion underlies the recent emergence of the notions of attochemistry [6] and charge-directed reactivity [7]. An important prototypical example, where fast electron motion plays a significant role, is in the sudden (or *impulsive*) ionization of a molecule.

Impulsive molecular ionization can be driven by high energy electrons, ions/cosmic rays, or photons and can initiate fragmentation and chemical change. Impulsive ionization of organic and small biomolecules is now widely acknowledged to lead to attosecond scale chemical processes [1] that are likely at work in ionizing environments in space [8], in planetary atmospheres and in tissue during radiation therapy. When a valence electron is suddenly removed from a molecule, by an attosecond soft x-ray pulse or a collision with a fast charged particle (e.g. a cosmic ray), it inevitably forms a superposition of electronic states of the cation, i.e. an *electronic wavepacket*. Basic quantum mechanics tells us that this electronic wavepacket can lead to oscillation in the electronic density, which has been termed charge migration. This purely electronic charge migration results from the coherent superposition of the stationary electronic eigenstates. For the valence electrons of small molecules, the energy splitting between states composing the wavepacket is on the scale of an electron volt (eV)[9], corresponding to electron motion on few-femtosecond (fs) to attosecond (as) timescales. The oscillatory charge motion leads to new time-dependent forces absent under conventional 'slow' ionization associated with a single electronic state [10, 11], and will therefore induce unique new vibronic modes and dynamics of fragmentation [12, 13, 14]. This channel of *attochemical* activity is not well explored due to the challenge of producing suitably fast excitations for impulsive initiation and/or subsequent probing of the unfolding electronic and nuclear dynamics. This ultrafast electron motion is expected to directly impact the breaking and forming of chemical bonds in the ionic products, but the mechanisms and consequences of these reactions continue to be inaccessible to most measurements.

Several pioneering measurements based on high harmonic generation [15] have provided insight into electron dynamics on the attosecond timescale. A pair of ultraviolet (UV) attosecond pulse

trains has been used to probe electron dynamics in nitrogen molecules [16] and a pair of single-femtosecond UV pulses was used to observe electron motion in xenon atoms [17]. Recently, a two-color UV attosecond pulse-pair was employed to time-resolve the creation of the argon cation [18]. Further measurements of ultrafast charge motion, which extend to more complex molecular systems, have made use of strong-field interactions to initiate [19, 20, 21] or interrogate [22, 20, 23, 24, 25, 26] few-femtosecond scale charge motion in molecules. The effect of a strong laser field on the molecular system is, however, challenging to interpret because the interaction with the field is highly non-perturbative, and many observables rely on long-term outcomes such as molecular fragmentation, which introduces additional complexity to numerical modeling.

X-ray observables, on the other hand, are more easily modeled and interpreted [27, 28, 29, 30, 31] and importantly, x-rays also address core-to-valence transitions and therefore probe the valence electron density in the vicinity of the atomically-localized core-level electrons. This has been demonstrated in recent experiments using degenerate [13, 14] or near-degenerate [32] few-femtosecond x-ray pulse pairs to probe electronic motion. However, the use of few-femtosecond x-ray pulses in these experiments does not provide an easily interpretable measurement of the sub-femtosecond impulsive response of a molecule.

In our measurements, we employ attosecond x-ray pulse-pairs to access the sub-femtosecond electron dynamics following impulsive photoionization of the aromatic molecule para-aminophenol. We probe the time-dependent electron density at the oxygen site *via* time-resolved x-ray absorption spectroscopy (trXAS) at the oxygen K-edge, employing the yield of resonant Auger-Meitner electrons to measure the absorption amplitude [31]. We compare our measurement with state-of-the-art computational modeling of the interaction between the molecule and both the pump and probe x-ray pulses. Our study reveals the nature of the molecular response to impulsive ionization, which involves multiple timescales, as shown in Figure 1. We observe sub-femtosecond population dynamics due to non-radiative, super-Coster-Kronig decay, and few-femtosecond oscillatory electron motion associated with stable cation states. We attribute the overall decay of this oscillatory signal to the effect of nuclear motion on the few-femtosecond timescale, providing insight into the earliest stages of photochemistry in the studied molecule.

The charge distribution of an impulsively excited molecule can undergo rapid non-equilibrium motion [33] through coherent population of a superposition of eigenstates. For several decades,

this motion has been approximated within the paradigm of 'charge migration', in which motion is driven solely by a coherent superposition of electronic states of ionized molecules [34]. An example of this type of motion is calculated and shown in Figure 2, which shows the response of the para-aminophenol molecule following impulsive valence ionization by an attosecond x-ray pulse, in the fixed-nuclei approximation. Ionization by this pulse, which has a large bandwidth and can address a broad manifold of inner- and outer-valence orbitals, populates a superposition of delocalized electronic states in the cation. The coherent evolution of this superposition causes the hole density to migrate across the molecule (Figure 2b showing snapshots at 5.7 and 6.8 fs), resulting in an oscillation of the hole density at the oxygen site (Figure 2c).

The charge migration paradigm described above has motivated experiments on extreme timescales to understand the first moments of photochemistry [35]. However, many aspects of attosecond electron motion following impulsive molecular excitation remain unexplored, such as the mechanism and timescale for electronic decoherence and how electron motion couples to nuclear motion that can drive chemical bond rearrangement [6, 1, 36, 37]. To address this scientific challenge, in this work we use a pair of attosecond x-ray pulses from a free-electron laser to resolve ultrafast electron motion with attosecond temporal resolution and Ångstrom-scale spatial sensitivity, without perturbing the dynamics with the probe field. Figure 2c shows a comparison between the time-resolved x-ray absorption signal below the oxygen K-edge (523–529 eV, green curve) and the oscillating portion of the hole charge localized at the oxygen atom (black curves) following ionization by a sub-femtosecond (700 as full-width at half maximum), $\sim$ 260 eV x-ray pulse. The two calculated curves follow each other closely, illustrating the power of x-ray observables to probe the local electronic density on sub-femtosecond timescales.

Two-color ($\omega/2\omega$) attosecond x-ray pulse pairs were generated at the Linac Coherent Light Source (LCLS) XFEL using a harmonic configuration of the split-undulator method [38, 39], which is illustrated in Figure 3a. The delay between the pump (ω) and probe (2ω) pulses was controlled by changing the number of undulators used to produce the probe pulse, and adjusting the magnetic chicane that sits between the two undulator sections producing the pump and probe pulses [39] (see Methods). The x-ray absorption signal was measured by recording the photon-energy-dependent electron emission from the molecule using a magnetic bottle electron spectrometer [40]. The photon-energy-resolved electron emission spectrum for the ground state molecule is shown in Figure 3c.

The photoemission spectrum is dominated by several strong features within $\sim 470 - 510$ eV kinetic energy. When the incoming photon energy is below the oxygen K-edge at 539 eV [41], these electrons are associated with resonant Auger-Meitner decay following $1s \rightarrow$valence absorption at ~ 532 eV. Above the oxygen K-edge, these electrons are produced by non-resonant (KLL) Auger-Meitner decay following K-shell ionization of the ground state molecule. A much weaker signal from direct valence ionization can be seen as a faint, dispersive streak with $\sim 480 - 500$ eV kinetic energy at 510 eV photon energy and increasing kinetic energy with increasing photon energy. In our measurements, the total electron yield is directly proportional to the x-ray absorption. To enhance the spectral resolution of our x-ray absorption measurement, we performed a shot-to-shot characterization of the incident x-ray spectrum coincident with the Auger-Meitner electron yield, using a variable line spacing (VLS) grating x-ray spectrometer [42] downstream of the interaction region, as shown in Figure 3a.

The pump pulse was tuned to ~260 eV, with a a full-width-at-half-maximum (FWHM) bandwidth of 2.4 eV. This photon energy is below the ionization potential for the carbon, nitrogen and oxygen K-shells of the molecule, so the pump pulse can only remove an electron from the valence orbitals. We then probed the ultrafast electron motion by measuring the x-ray absorption spectrum in the vicinity of the oxygen K-edge, by scanning the central photon energy of the probe pulse from $500 - 530$ eV for each pump-probe delay. A simplified schematic of the experimental protocol is illustrated in Figure 3d. The electron hole created by the pump pulse produces a new feature in the oxygen K-shell absorption spectrum. Figure 2c shows that the strength of this absorption feature is predicted to depend on the localization of the hole at the oxygen atom. The core-excited ion produced by the core-to-valence absorption decays *via* Auger-Meitner emission, emitting a broad spectrum of electrons with kinetic energies between $470 - 510$ eV. The sample absorption is given by the yield of these Auger-Meitner electrons.

Attosecond x-ray free-electron lasers rely on the process of self-amplified spontaneous emission (SASE), where the x-ray pulse builds up from stochastic noise in the electron bunch [43]. We exploit the resultant spectral fluctuations to achieve sub-bandwidth spectral resolution in the trXAS measurement using spectral domain ghost imaging [44]. In addition to fluctuations in the spectrum of the FEL, there are shot-to-shot fluctations in the pump and probe pulse energy. In order to extract the two-photon pump-probe signal, the data were binned according to the total pulse energy of the

pump pulse, and we measure the x-ray absorption spectrum at the oxygen K-edge for each pump pulse energy bin. The center of the bins range from 6 μJ to 85 μJ. The x-ray absorption spectra for different pump pulse energies are shown in Figure 3f for a pump-probe delay of 5.4 fs. A transient feature with a linear dependence on pump pulse energy appears in the probe absorption spectrum between 523 to 529 eV, shaded in blue in Figure 3f. We extracted the pump-probe trXAS signal by regressing the total absorption in this region of interest on pump pulse energy, as shown in the inset of Figure 3f. Negligible absorption was measured in the ground state molecule between 505 and 530 eV (this is shown as the gray curve in Figure 4b). We did not record sufficient data to resolve the absorption spectrum for probe photon energies above 530 eV since the electron detector was saturated by ionizing the ground state of the molecule at these photon energies.

We now turn to the main experimental result of this work, namely the measurement of time-dependent electron densities in the vicinity of the oxygen-site. Scanning the undulator gap along with the intrinsic photon energy fluctuation of the enhanced SASE process enabled us to scan the photon energy between 510 – 529 eV, allowing us to simultaneously explore the dynamical response for different probe photon energies. We analyzed the delay-dependence of the x-ray absorption below 523 eV (green and red traces in Fig. 3g). Between 517–523 eV (green) we observed no delay-dependence in the absorption. Between 510–517 eV (red), we observed weak evidence of a sub-femtosecond decay, but the signal is very close to the noise floor of the measurement. This contrasts with the delay dependence for probe photons in the range 523-529 eV (blue curve), which corresponds to the photon energy where we expect the absorption for low-lying cationic states to be observed. The delay-dependent pump-probe signal in the transient spectral feature, shown as the blue trace in Figure 3g, decays rapidly within the first 2 fs and exhibits a revival around 5 fs. By approximately 10 fs, the pump-probe signal has decayed to zero. The contrast of behavior between the blue and the red and green curves in Figure 3g, combined with our evaluated error bounds, corroborates the significance of our observation of the temporal dependence in the valence hole excitation region indicative of oscillatory charge migration dynamics.

To understand the time-dependence of the pump-probe absorption signal, we compare our experimental results with *ab initio* calculations of both the valence-induced electron dynamics and their associated x-ray absorption signatures. We employed two state-of-the-art numerical approaches to evaluate the experimental observables following the interaction of the molecule

with the pump and probe pulses, and directly compare our experimental results with theoretical predictions. We label the two numerical methods as "ADC" (algebraic diagrammatic construction) and "RAS-SXD" (restricted active space static-exchange B-spline density functional theory). Both methods solve the time-dependent Schrödinger equation for the system interacting with the pump pulse. Following the pump interaction, the photoelectron degree of freedom is traced out. We then solve the von Neumann equation to calculate the evolution of the system until the end of the probe pulse. The two methods use a different description for both the bound electronic states of the molecule and the continuum, as well as the interaction terms used to model the effect of the pump pulse (see **Methods** and supplementary materials).

The calculated x-ray photoelectron binding energy spectrum produced by the pump pulse is compared to our measurement in Figure 4a. We find satisfactory agreement between the measured and predicted photoelectron spectrum using both computation methods, however, the RAS-SXD method provides better agreement for states above the DIP. This likely reflects the lower number of cationic used in the ADC calculation compared to the RAS-SXD. Next we compare the measured and calculated time-resolved x-ray absorption spectra at short pump-probe delays (< 2 fs), in Figure 4b. Both methods predict that the absorption feature produced by the interaction with the pump-pulse contains comparable contributions from cationic states energetically below and above the double ionization potential (DIP) of the molecule (21 eV), as shown in Figure 4b. There is significant energetic overlap, which is larger in the RAS-SXD model, between the absorption signal for these two sets of states. The energies of the strongest x-ray absorption transitions are found to be similar for states above and below the DIP in the ADC and RAS-SXD calculations. For states above the DIP, the probe dipole coupling is therefore strongest for higher-lying satellite states. States above the DIP are open to rapid autoionization *via* super-Coster-Kronig decay [45], in which the vacancy is filled by an electron from the same shell, resulting in emission of another electron. This autoionization process, which is illustrated in Figure 4d, typically occurs on the sub-femtosecond timescale and has not previously been resolved in the time domain. We simulate the energy-dependent lifetimes for super-Coster-Kronig decay to be between $0.35 - 0.86$ fs with the Fano-ADC(2,2) method [46], see supplementary materials for details.

The simulated delay-dependent XAS observable is shown in Figure 4c. Both simulations predict few-femtosecond oscillations in the absorption signal, driven by the electronic coherence imparted

by the pump pulse. Strikingly, both the characteristic modulation frequency and the modulation depth are very different for the two methods. The general agreement between both the calculated pump photoelectron and our experimental measurement (Figure 4a), suggests that the photoionization cross sections, or the magnitude of the ionization amplitudes, do not strongly differ between the two calculations. Then the discrepancy in the time-dependent traces indicates it is the phase of the ionization amplitudes that differs between calculations. These phase differences are sensitive to small differences in the electronic wavefunctions and rely critically on the description of both the bound and continuum wavefunctions. The predicted time-domain signal may also be sensitive to the inclusion of interchannel coupling between the photoelectron and the cation, in the ADC simulation of the pump ionization step [47]. This discrepancy between the time-domain predictions of our two state-of-the-art numerical approaches highlights the advantage of time-domain measurements for differentiating and optimizing high-level models ofelectronic motion following excitation by a broad bandwidth pulse.

To compare with the simulated observables with the measured data, we convolve the numerical calculations with a gaussian kernel of $\sigma = 150$ as, to account for the measured jitter in the pump/probe delay [39]. Comparing the result in Fig. 4c, it is clear that this level of jitter will not affect the interpretation of the measurement. In Figure 4e we directly compare the simulated trXAS signals with our measurement. We scale the absolute magnitude of the simulated trXAS signals independently to achieve the best overall agreement between the first 4 time-points of the experimental data. The signal within the region of temporal overlap of the two pulses (delays shorter than the gray shaded region in Fig. 4e) is challenging to simulate, and is approximated by by assuming separable pump and probe interactions, i.e., that the electrons ionized by the pump pulse instantly leave the system unaffected by the remainder of the pump pulse and that the probe pulse exclusively interacts with the created cation (see methods). The comparison with the calculations guide us to assign the increase in the measured absorption at 5.4 fs to a transient revival of valence hole density in the vicinity of the oxygen atom driven by coherent electron motion. Both theories show acceptable agreement with the first 4 experimental points, with the ADC approach predicting a larger contrast in the coherent oscillation leading a better agreement with the experimental trXAS, in particular for the delay of at 1.9 fs. This highlights the fact that the differentiation of theoretical models requires measurements which are sensitive to both the amplitude and the relative phase of

the excited states.

The measurement shows a rapid decay of the trXAS signal within the first femtosecond. We partially attribute this rapid decay to the super-Coster-Kronig effect, which results in almost complete depopulation of states above the DIP within the first femtosecond. This process is incorporated in our calculations as a phenomenological decay of the populations of the states above the DIP with the aforementioned lifetimes of 0.35 fs – 0.86 fs (see Supplementary Information). The additional absorption from dication states populated through autoionization is also included in the simulated trXAS signal. For delays above 1.7 fs, our simulations indicate that the x-ray absorption in the dication may partially compensate the decrease in the cation absorption. We expect this rapid initial decay to be a general feature of the impulsive response of a molecule to ionization by broad-bandwidth light.

An additional feature in our experimental result is a decay in the overall XAS signal after roughly 5 fs, which is not well represented by either numerical method in Figure 4e. Although the measurements cannot rule out that there may be a revival at a later time, this feature is likely a result of fast nuclear motion in the vicinity of the oxygen atom, for example proton loss, which is not accounted for in our simulations and may quench, shift or broaden the absorption feature shown in Figure 4b. Nonadiabatic electron-nuclear dynamics can also affect the absorption spectrum by modulating the excited state populations [48, 49]. We investigate this overall decay by incorporating an empirical decay term in the calculated XAS signal. A simple exponential model can account for population decay, a shift or broadening of the absorption feature, and pure dephasing of a two-level system [50]. We use the ADC calculation to find the overall decay constant, which is 6.8 fs, that best matches our measurement by fitting the decay and scaling coefficients of the exponential decay model to the third through ninth delay points where nuclear dynamics would be the most relevant. We find that incorporating this decay term for both simulated trXAS traces, shown in Figure 4e as the solid lines, improves the agreement between theory and experiment. A shift in the absorption feature caused by proton loss is consistent with observations as well as physically reasonable. This highlights the need for complex modeling of effects such as nuclear motion and electron-nuclear coupling, to fully describe ultrafast charge motion on the sub- to few-femtosecond timescale.

Conclusion

We have performed an attosecond x-ray pump/attosecond x-ray probe measurement of the response of a para-aminophenol molecule to impulsive valence shell ionization. Following ionization by the pump pulse, a transient feature was observed in the x-ray absorption spectrum roughly ~20 eV below the oxygen K-edge of the neutral molecule. By monitoring the delay-dependence of this absorption feature, we probed the time-evolving electron density in the molecule from the instant of photoionization with attosecond time resolution and atomic site specificity. The tuning of the probe gives us sensitivity to the full spectrum of valence shell vacancy states, so that we can probe the dynamics of the hole dynamics near the oxygen-site.

We observe evidence for three distinct timescales: the decay of states above the DIP within the first femtosecond, the few-femtosecond coherent dynamics associated with coherently populated states of the cation, and the reduction of the signal over 5-10 fs, which we tentatively associate with the onset of nuclear motion. We expect this behavior to be general to small molecules, not only in the case of photoionization but also in response to fast ion or electron ionization of the valence shell, where the impulsive limit is reached. Our work provides insight into the earliest stages of ionization-induced chemistry and highlights the need to further explore the impact of coherent electronic phenomena on the resulting coupling of nuclear and electronic motion and subsequent chemical processes. X-ray attosecond pump/probe spectroscopy provides the experimental framework to do this in a broad range of molecular systems by achieving atomic specificity and attosecond time resolution. The benchmark data provided from such measurements as this one will underpin advances in computational chemistry approaches with impact across photochemistry. Our method also points the way to future studies that combine synchronized optical or X-ray Raman excitation with x-ray probes to directly address ultrafast photochemistry in neutral systems.

Methods

Two-Pulse X-ray Generation

Attosecond $\omega/2\omega$ pulse pairs with controllable delays down to the sub-femtosecond level were generated at the LCLS by lasing a high current spike in the split-undulator mode [39]. The high

current spike in the electron bunch was produced by shaping the temporal profile of the photocathode laser [51]. Single-spike attosecond soft x-ray pulses were generated by lasing this high current spike in the downstream undulator beamline. In the split-undulator mode, the same electron beam generates the pump and probe pulses in two different undulator sections, which are separated by a magnetic chicane [52]. Since the same electron bunch is used to generate the pump and probe pulses, the time delay between the pulses is independent of the electron beam arrival time jitter and therefore remains very stable [39]. The undulator parameters K in the two undulator sections were tuned separately to produce attosecond $\hbar\omega$~260 eV and $2\hbar\omega$~520 eV pulses in the first and the second undulator sections, respectively. The time delay between the pump and probe pulses was controlled by tuning the magnetic chicane and the number of undulator modules used (i.e. set on resonance with the 2ω probe pulse) in the second undulator section. In the harmonic lasing setup employed here, the strong microbunching produced in the high current spike during the generation of the pump (ω) pulse was amplified in the generation of the probe (2ω) pulse. This ensured the power of the probe pulses was amplified to above GW-level in a short undulator distance, avoiding long slippage lengths and enabling sub-femtosecond pump-probe delays.

The time delays between pump/probe pulse pairs at a different photon energy setup (370 eV/740 eV) were measured in a separate experiment using the angular streaking technique [39]. We performed detailed time-dependent XFEL simulations to benchmark the time delays we measured in the angular streaking experiment and studied the dependence of the time delays on electron beam parameters, undulator beamline configurations, and XFEL photon energies. To calculate the time delays for our trXAS experiment, we employed the time-dependent XFEL simulations which we had previously benchmarked with our angular streaking measurements. We set the central energy of the electron bunch to 4.08 GeV and adjusted the undulator matching condition to match the parameters used in the trXAS experiment, and simulated the average time delays for each beamline delay configuration that we used. The uncertainty in the simulated average time delays in the trXAS experiment was estimated by scaling the emittance of the electron bunch used in the numerical simulation. The maximal (minimal) emittance scaling ratio was determined by scaling the emittance until the simulated ω pulse energy reduced (increased) by a factor of 2. Six values of emittance scaling ratio were taken between the maximal and minimal values, and an average time delay between $\omega/2\omega$ pulse pairs was calculated for each beamline configuration (i.e. pump/probe

delay) for each emittance scaling ratio. The systematic uncertainty of the simulated average delay at a given beamline configuration, shown as the horizontal errorbar in Figures 3g and 4e in the main text, was the standard deviation of these six simulated average delays.

Experimental Setup

The measurements were performed at the time-resolved molecular, and optical science (TMO) experimental hutch of the LCLS [53]. The x-ray pulses were focused using a pair of Kirkpatrick-Baez focusing mirrors [54]. The para-aminophenol sample was introduced using an in-vacuum oven heated to $\sim$ 160 °C. The focused x-ray beam intercepted the molecular sample in the interaction region of a two-meter magnetic bottle electron time-of-flight spectrometer (MBES) [40]. For the trXAS measurements, a static 400 V retardation voltage was applied to the flight tube of the MBES to increase the kinetic energy resolution for the Auger-Meitner electrons. The electrons were detected using a micro-channel plate detector coupled to a segmented anode. The spectrum of the probe pulse was measured shot-to-shot by a variable line spacing (VLS) grating spectrometer [42]. Since the gas-phase para-aminophenol sample was very dilute, the x-ray pulse experienced negligible attenuation through the sample and the spectral measurement made downstream of the interaction point was faithful to the incoming spectrum.

Data Analysis

We use spectral domain ghost imaging to retrieve the x-ray absorption cross section with sub-bandwidth resolution [44]. In the present implementation, this technique is equivalent to multiple linear regression. The natural variation of a self-amplified spontaneous emission (SASE) XFEL, along with the variation induced by scanning the undulator K-value, creates shot-to-shot changes in the photon spectrum and we extract the correlation between the incident x-ray spectra and the response (in this case, yield of resonant Auger-Meitner electrons) of the gas-phase sample. For a given pump pulse energy, the x-ray absorption is linearly related to the spectrum of the probe pulse. The corrected probe absorption signal (see section 2 of the supplementary materials) for a given pump pulse energy bin, $\vec{\tilde{b}}$, can therefore be written as the inner product of the single-shot photon spectrum, $\mathbf{A}$, with the unknown sample absorption, $\vec{x}$: $\vec{\tilde{b}} = \mathbf{A}\vec{x}$. We can estimate the sample

absorption, $\vec{x}$, by minimizing the squared difference between the estimated sample absorption and the measured sample absorption, given by

$$||\mathbf{A}_{i,\omega}\vec{x}_{\omega} - \tilde{\vec{b}}_i||_2^2, \tag{1}$$

where ω is the probe photon-energy index and i is the shot index. We removed shots with a central probe photon energy outside the range 509.5 – 532.5 eV. As a result, the mean spectrum of the probe pulse was similar across different delay points.

To evaluate the trXAS signal, which is bilinear in the intensity of the pump and probe pulses, the data is binned into 10 pump pulse energy bins such that each bin contains an equal number of shots and the sample absorption, $\vec{x}$, is calculated for each pump pulse energy bin (left hand side of Extended Data Fig. E1). The absorption is then integrated across the resonance region from 523 eV to 529 eV, which is shown by the blue shaded region in Extended Data Fig. E1. Error bars for the integrated absorption yield are determined by re-sampling the data using bootstrap resampling (100 resamples). We then calculated the trXAS signal by calculating the slope of the absorption as a function of pump pulse energy, as shown in Extended Data Fig. E2. Error bars in the trXAS signal are the standard error of the slope, given by the covariance matrix found when we regressed the integrated absorption on the pump pulse energy. We enforced an upper limit on the probe pulse energy, by removing shots for which the probe pulse energy was higher than the value at which we observed evidence for saturation in our electron detection scheme.

Numerical Simulation

The ADC approach employs the time-dependent B-spline Restricted Correlation Space-Algebraic Diagrammatic Construction (RCS-ADC) method [55, 9, 47]. The time-dependent many-electron wavefunction is expanded on the basis of ground and excited RCS-ADC(2x) states, where the "(2x)" indicates the inclusion of the configuration space of two-hole, two-particle states. This expansion incorporates terms that describe interchannel coupling between different ionic states as the photoelectron departs the cation. Within the RAS-SXD approach, we use multi-configurational restricted active space self-consistent field (RASSCF) wavefunctions to describe the bound molecular states, with dynamic correlation included perturbatively (RASPT2) [56]. The pump pulse populates

single-channel continua, with the continuum orbitals described by static-exchange B-spline density functional theory (SXD) [57, 58, 59]. Both calculations are performed at the equilibrium geometry of neutral para-aminophenol. The numerical methods are described in detail in the supplementary materials.

References and Notes

[1] Francesca Calegari and Fernando Martin. Open questions in attochemistry. *Communications Chemistry*, 6(1):1–5, September 2023. Number: 1 Publisher: Nature Publishing Group.

[2] Oksana Ostroverkhova. Organic Optoelectronic Materials: Mechanisms and Applications. *Chemical Reviews*, 116(22):13279–13412, November 2016. Publisher: American Chemical Society.

[3] Mark I Stockman, Katrin Kneipp, Sergey I Bozhevolnyi, Soham Saha, Aveek Dutta, Justus Ndukaife, Nathaniel Kinsey, Harsha Reddy, Urcan Guler, Vladimir M Shalaev, Alexandra Boltasseva, Behrad Gholipour, Harish N S Krishnamoorthy, Kevin F MacDonald, Cesare Soci, Nikolay I Zheludev, Vassili Savinov, Ranjan Singh, Petra Groß, Christoph Lienau, Michal Vadai, Michelle L Solomon, David R Barton, Mark Lawrence, Jennifer A Dionne, Svetlana V Boriskina, Ruben Esteban, Javier Aizpurua, Xiang Zhang, Sui Yang, Danqing Wang, Weijia Wang, Teri W Odom, Nicolò Accanto, Pablo M de Roque, Ion M Hancu, Lukasz Piatkowski, Niek F van Hulst, and Matthias F Kling. Roadmap on plasmonics. *Journal of Optics*, 20(4):043001, mar 2018.

[4] Martin Schultze, Krupa Ramasesha, C.D. Pemmaraju, S.A. Sato, D. Whitmore, A. Gandman, James S. Prell, L. J. Borja, D. Prendergast, K. Yabana, Daniel M. Neumark, and Stephen R. Leone. Attosecond band-gap dynamics in silicon. *Science*, 346(6215):1348–1352, 2014.

[5] J. Freudenstein, M. Borsch, M. Meierhofer, D. Afanasiev, C. P. Schmid, F. Sandner, M. Liebich, A. Girnghuber, M. Knorr, M. Kira, and R. Huber. Attosecond clocking of correlations between Bloch electrons. *Nature*, 610(7931):290–295, October 2022.

[6] Franck Lépine, Misha Y. Ivanov, and Marc J. J. Vrakking. Attosecond molecular dynamics: fact or fiction? *Nature Photonics*, 8(3):195–204, March 2014.

[7] F. Remacle, R. D. Levine, and M. A. Ratner. Charge directed reactivity:: a simple electronic model, exhibiting site selectivity, for the dissociation of ions. *Chemical Physics Letters*, 285(1–2):25–33, March 1998.

[8] A. G. G. M. Tielens. The molecular universe. *Rev. Mod. Phys.*, 85:1021–1081, Jul 2013.

[9] M Ruberti. Onset of ionic coherence and ultrafast charge dynamics in attosecond molecular ionisation. *Physical Chemistry Chemical Physics*, 21(32):17584–17604, 2019.

[10] Don Danilov, Thierry Tran, Michael J. Bearpark, Jon P. Marangos, Graham A. Worth, and Michael A. Robb. How electronic superpositions drive nuclear motion following the creation of a localized hole in the glycine radical cation. *The Journal of Chemical Physics*, 156(24):244114, June 2022. Publisher: American Institute of Physics.

[11] Manuel Cardosa-Gutierrez, R D Levine, and F Remacle. Electronic coherences built by an attopulse control the forces on the nuclei. *Journal of Physics B: Atomic, Molecular and Optical Physics*, 57(13):133501, June 2024. Publisher: IOP Publishing.

[12] Anthony Ferté, Dane Austin, Allan S. Johnson, Felicity McGrath, João Pedro Malhado, Jon P. Marangos, and Morgane Vacher. Signature of Attochemical Quantum Interference upon Ionization and Excitation of an Electronic Wave Packet in Fluorobenzene. *Physical Review Letters*, 133(20):203201, November 2024. Publisher: American Physical Society.

[13] David Schwickert, Marco Ruberti, Přemysl Kolorenč, Sergey Usenko, Andreas Przystawik, Karolin Baev, Ivan Baev, Markus Braune, Lars Bocklage, Marie Kristin Czwalinna, Sascha Deinert, Stefan Düsterer, Andreas Hans, Gregor Hartmann, Christian Haunhorst, Marion Kuhlmann, Steffen Palutke, Ralf Röhlsberger, Juliane Rönsch-Schulenburg, Philipp Schmidt, Sven Toleikis, Jens Viefhaus, Michael Martins, André Knie, Detlef Kip, Vitali Averbukh, Jon P. Marangos, and Tim Laarmann. Electronic quantum coherence in glycine molecules probed with ultrashort x-ray pulses in real time. *Science Advances*, 8(22):eabn6848, June 2022. Publisher: American Association for the Advancement of Science.

[14] David Schwickert, Marco Ruberti, Přemysl Kolorenč, Andreas Przystawik, Slawomir Skruszewicz, Malte Sumfleth, Markus Braune, Lars Bocklage, Luis Carretero, Marie Kristin Czwalinna, Dian Diaman, Stefan Düsterer, Marion Kuhlmann, Steffen Palutke, Ralf Röhlsberger, Juliane Rönsch-Schulenburg, Sven Toleikis, Sergey Usenko, Jens Viefhaus, Anton Vorobiov, Michael Martins, Detlef Kip, Vitali Averbukh, Jon P. Marangos, and Tim Laarmann. Charge-induced chemical dynamics in glycine probed with time-resolved Auger elec-

tron spectroscopy. *Structural Dynamics*, 9(6):064301, November 2022. Publisher: American Institute of Physics.

[15] M. Ferray, A. L'Huillier, X. F. Li, L. A. Lompre, G. Mainfray, and C. Manus. Multiple-harmonic conversion of 1064 nm radiation in rare gases. *Journal of Physics B: Atomic, Molecular and Optical Physics*, 21(3):L31, February 1988.

[16] Tomoya Okino, Yusuke Furukawa, Yasuo Nabekawa, Shungo Miyabe, A. Amani Eilanlou, Eiji J. Takahashi, Kaoru Yamanouchi, and Katsumi Midorikawa. Direct observation of an attosecond electron wave packet in a nitrogen molecule. *Science Advances*, 1(8):e1500356, September 2015.

[17] P. Tzallas, E. Skantzakis, L. a. A. Nikolopoulos, G. D. Tsakiris, and D. Charalambidis. Extreme-ultraviolet pump–probe studies of one-femtosecond-scale electron dynamics. *Nature Physics*, 7(10):781–784, October 2011. Number: 10 Publisher: Nature Publishing Group.

[18] Martin Kretschmar, Evaldas Svirplys, Mikhail Volkov, Tobias Witting, Tamás Nagy, Marc J. J. Vrakking, and Bernd Schütte. Compact realization of all-attosecond pump-probe spectroscopy. *Science Advances*, 10(8):eadk9605, February 2024. Publisher: American Association for the Advancement of Science.

[19] Eleftherios Goulielmakis, Zhi-Heng Loh, Adrian Wirth, Robin Santra, Nina Rohringer, Vladislav S. Yakovlev, Sergey Zherebtsov, Thomas Pfeifer, Abdallah M. Azzeer, Matthias F. Kling, Stephen R. Leone, and Ferenc Krausz. Real-time observation of valence electron motion. *Nature*, 466(7307):739–743, August 2010.

[20] P. M. Kraus, B. Mignolet, D. Baykusheva, A. Rupenyan, L. Horný, E. F. Penka, G. Grassi, O. I. Tolstikhin, J. Schneider, F. Jensen, L. B. Madsen, A. D. Bandrauk, F. Remacle, and H. J. Wörner. Measurement and laser control of attosecond charge migration in ionized iodoacetylene. *Science*, 350(6262):790–795, November 2015.

[21] Danylo T. Matselyukh, Victor Despré, Nikolay V. Golubev, Alexander I. Kuleff, and Hans Jakob Wörner. Decoherence and revival in attosecond charge migration driven by

non-adiabatic dynamics. *Nature Physics*, 18(10):1206–1213, October 2022. Number: 10 Publisher: Nature Publishing Group.

[22] F. Calegari, D. Ayuso, A. Trabattoni, L. Belshaw, S. De Camillis, S. Anumula, F. Frassetto, L. Poletto, A. Palacios, P. Decleva, J. B. Greenwood, F. Martín, and M. Nisoli. Ultrafast electron dynamics in phenylalanine initiated by attosecond pulses. *Science*, 346(6207):336–339, October 2014.

[23] Manuel Lara-Astiaso, Mara Galli, Andrea Trabattoni, Alicia Palacios, David Ayuso, Fabio Frassetto, Luca Poletto, Simone De Camillis, Jason Greenwood, Piero Decleva, Ivano Tavernelli, Francesca Calegari, Mauro Nisoli, and Fernando Martín. Attosecond Pump–Probe Spectroscopy of Charge Dynamics in Tryptophan. *The Journal of Physical Chemistry Letters*, pages 4570–4577, July 2018.

[24] E. Perfetto, A. Trabattoni, F. Calegari, M. Nisoli, A. Marini, and G. Stefanucci. Ultrafast Quantum Interference in the Charge Migration of Tryptophan. *The Journal of Physical Chemistry Letters*, 11(3):891–899, February 2020. Publisher: American Chemical Society.

[25] Erik P. Månsson, Simone Latini, Fabio Covito, Vincent Wanie, Mara Galli, Enrico Perfetto, Gianluca Stefanucci, Hannes Hübener, Umberto De Giovannini, Mattea C. Castrovilli, Andrea Trabattoni, Fabio Frassetto, Luca Poletto, Jason B. Greenwood, François Légaré, Mauro Nisoli, Angel Rubio, and Francesca Calegari. Real-time observation of a correlation-driven sub 3 fs charge migration in ionised adenine. *Communications Chemistry*, 4(1):1–7, May 2021. Number: 1 Publisher: Nature Publishing Group.

[26] Erik P. Månsson, Simone Latini, Fabio Covito, Vincent Wanie, Mara Galli, Enrico Perfetto, Gianluca Stefanucci, Umberto De Giovannini, Mattea C. Castrovilli, Andrea Trabattoni, Fabio Frassetto, Luca Poletto, Jason B. Greenwood, François Légaré, Mauro Nisoli, Angel Rubio, and Francesca Calegari. Ultrafast dynamics of adenine following XUV ionization. *Journal of Physics: Photonics*, 4(3):034003, May 2022. Publisher: IOP Publishing.

[27] Min Chen and Kenneth Lopata. First-Principles Simulations of X-ray Transient Absorption for Probing Attosecond Electron Dynamics. *Journal of Chemical Theory and Computation*, May 2020. Publisher: American Chemical Society.

[28] Anthony D. Dutoi and Lorenz S. Cederbaum. Time-resolved pump-probe spectroscopy to follow valence electronic motion in molecules: Application. *Physical Review A*, 90(2):023414, August 2014.

[29] Francesco Segatta, Artur Nenov, Silvia Orlandi, Alberto Arcioni, Shaul Mukamel, and Marco Garavelli. Exploring the capabilities of optical pump X-ray probe NEXAFS spectroscopy to track photo-induced dynamics mediated by conical intersections. *Faraday Discussions*, 221(0):245–264, December 2019. Publisher: The Royal Society of Chemistry.

[30] Simon P. Neville, Majed Chergui, Albert Stolow, and Michael S. Schuurman. Ultrafast X-Ray Spectroscopy of Conical Intersections. *Physical Review Letters*, 120(24):243001, June 2018.

[31] Bridgette Cooper, Přemysl Kolorenč, Leszek J. Frasinski, Vitali Averbukh, and Jon P. Marangos. Analysis of a measurement scheme for ultrafast hole dynamics by few femtosecond resolution X-ray pump–probe Auger spectroscopy. *Faraday Discussions*, 171(0):93–111, November 2014.

[32] T. Barillot, O. Alexander, B. Cooper, T. Driver, D. Garratt, S. Li, A. Al Haddad, A. Sanchez-Gonzalez, M. Agåker, C. Arrell, M. J. Bearpark, N. Berrah, C. Bostedt, J. Bozek, C. Brahms, P. H. Bucksbaum, A. Clark, G. Doumy, R. Feifel, L. J. Frasinski, S. Jarosch, A. S. Johnson, L. Kjellsson, P. Kolorenč, Y. Kumagai, E. W. Larsen, P. Matia-Hernando, M. Robb, J.-E. Rubensson, M. Ruberti, C. Sathe, R. J. Squibb, A. Tan, J. W. G. Tisch, M. Vacher, D. J. Walke, T. J. A. Wolf, D. Wood, V. Zhaunerchyk, P. Walter, T. Osipov, A. Marinelli, T. J. Maxwell, R. Coffee, A. A. Lutman, V. Averbukh, K. Ueda, J. P. Cryan, and J. P. Marangos. Correlation-Driven Transient Hole Dynamics Resolved in Space and Time in the Isopropanol Molecule. *Physical Review X*, 11(3):031048, September 2021. Publisher: American Physical Society.

[33] Stephen R. Leone, C. William McCurdy, Joachim Burgdörfer, Lorenz S. Cederbaum, Zenghu Chang, Nirit Dudovich, Johannes Feist, Chris H. Greene, Misha Ivanov, Reinhard Kienberger, Ursula Keller, Matthias F. Kling, Zhi-Heng Loh, Thomas Pfeifer, Adrian N. Pfeiffer, Robin Santra, Kenneth Schafer, Albert Stolow, Uwe Thumm, and Marc J. J. Vrakking. What will it take to observe processes in 'real time'? *Nature Photonics*, 8(3):162–166, March 2014.

[34] L. S. Cederbaum and J. Zobeley. Ultrafast charge migration by electron correlation. *Chemical Physics Letters*, 307(3):205–210, July 1999.

[35] Ferenc Krausz and Misha Ivanov. Attosecond physics. *Reviews of Modern Physics*, 81(1):163–234, February 2009. Publisher: American Physical Society.

[36] Shoutian Sun, Benoit Mignolet, Lin Fan, Wen Li, Raphael D. Levine, and Francoise Remacle. Nuclear Motion Driven Ultrafast Photodissociative Charge Transfer of the PENNA Cation: An Experimental and Computational Study. *The Journal of Physical Chemistry A*, 121(7):1442–1447, February 2017. Publisher: American Chemical Society.

[37] Mauro Nisoli, Piero Decleva, Francesca Calegari, Alicia Palacios, and Fernando Martín. Attosecond Electron Dynamics in Molecules. *Chemical Reviews*, May 2017.

[38] Joseph Duris, Siqi Li, Taran Driver, Elio G. Champenois, James P. MacArthur, Alberto A. Lutman, Zhen Zhang, Philipp Rosenberger, Jeff W. Aldrich, Ryan Coffee, Giacomo Coslovich, Franz-Josef Decker, James M. Glownia, Gregor Hartmann, Wolfram Helml, Andrei Kamalov, Jonas Knurr, Jacek Krzywinski, Ming-Fu Lin, Jon P. Marangos, Megan Nantel, Adi Natan, Jordan T. O'Neal, Niranjan Shivaram, Peter Walter, Anna Li Wang, James J. Welch, Thomas J. A. Wolf, Joseph Z. Xu, Matthias F. Kling, Philip H. Bucksbaum, Alexander Zholents, Zhirong Huang, James P. Cryan, and Agostino Marinelli. Tunable isolated attosecond X-ray pulses with gigawatt peak power from a free-electron laser. *Nature Photonics*, 14(1):30–36, January 2020.

[39] Zhaoheng Guo, Taran Driver, Sandra Beauvarlet, David Cesar, Joseph Duris, Paris L. Franz, Oliver Alexander, Dorian Bohler, Christoph Bostedt, Vitali Averbukh, Xinxin Cheng, Louis F. DiMauro, Gilles Doumy, Ruaridh Forbes, Oliver Gessner, James M. Glownia, Erik Isele, Andrei Kamalov, Kirk A. Larsen, Siqi Li, Xiang Li, Ming-Fu Lin, Gregory A. McCracken, Razib Obaid, Jordan T. O'Neal, River R. Robles, Daniel Rolles, Marco Ruberti, Artem Rudenko, Daniel S. Slaughter, Nicholas S. Sudar, Emily Thierstein, Daniel Tuthill, Kiyoshi Ueda, Enliang Wang, Anna L. Wang, Jun Wang, Thorsten Weber, Thomas J. A. Wolf, Linda Young, Zhen Zhang, Philip H. Bucksbaum, Jon P. Marangos, Matthias F. Kling, Zhirong Huang, Peter Walter, Ludger Inhester, Nora Berrah, James P. Cryan, and Agostino Marinelli.

Experimental demonstration of attosecond pump–probe spectroscopy with an X-ray free-electron laser. *Nature Photonics*, 18(7):691–697, July 2024. Publisher: Nature Publishing Group.

[40] Kurtis Borne, Jordan T. O'Neal, Jun Wang, Erik Isele, Razib Obaid, Nora Berrah, Xinxin Cheng, Philip H. Bucksbaum, Justin James, Andrei Kamalov, Kirk A. Larsen, Xiang Li, Ming-Fu Lin, Yusong Liu, Agostino Marinelli, Adam M. Summers, Emily Thierstein, Thomas J. A. Wolf, Daniel Rolles, Peter Walter, James P. Cryan, and Taran Driver. Design and performance of a magnetic bottle electron spectrometer for high-energy photoelectron spectroscopy. *Review of Scientific Instruments*, 95(12):125110, 12 2024.

[41] V. Zhaunerchyk, M. Kamińska, M. Mucke, R. J. Squibb, J. H. D. Eland, M. N. Piancastelli, L. J. Frasinski, J. Grilj, M. Koch, B. K. McFarland, E. Sistrunk, M. Gühr, R. N. Coffee, C. Bostedt, J. D. Bozek, P. Salén, P. v d Meulen, P. Linusson, R. D. Thomas, M. Larsson, L. Foucar, J. Ullrich, K. Motomura, S. Mondal, K. Ueda, R. Richter, K. C. Prince, O. Takahashi, T. Osipov, L. Fang, B. F. Murphy, N. Berrah, and R. Feifel. Disentangling formation of multiple-core holes in aminophenol molecules exposed to bright X-FEL radiation. *Journal of Physics B: Atomic, Molecular and Optical Physics*, 48(24):244003, October 2015. Publisher: IOP Publishing.

[42] Razib Obaid, Christian Buth, Georgi L. Dakovski, Randolf Beerwerth, Michael Holmes, Jeff Aldrich, Ming-Fu Lin, Michael Minitti, Timur Osipov, William Schlotter, Lorenz S. Cederbaum, Stephan Fritzsche, and Nora Berrah. LCLS in—photon out: fluorescence measurement of neon using soft x-rays. *Journal of Physics B: Atomic, Molecular and Optical Physics*, 51(3):034003, January 2018. Publisher: IOP Publishing.

[43] R. Bonifacio, L. De Salvo, P. Pierini, N. Piovella, and C. Pellegrini. Spectrum, temporal structure, and fluctuations in a high-gain free-electron laser starting from noise. *Physical Review Letters*, 73(1):70–73, July 1994.

[44] Taran Driver, Siqi Li, Elio G. Champenois, Joseph Duris, Daniel Ratner, Thomas J. Lane, Philipp Rosenberger, Andre Al-Haddad, Vitali Averbukh, Toby Barnard, Nora Berrah,

Christoph Bostedt, Philip H. Bucksbaum, Ryan Coffee, Louis F. DiMauro, Li Fang, Douglas Garratt, Averell Gatton, Zhaoheng Guo, Gregor Hartmann, Daniel Haxton, Wolfram Helml, Zhirong Huang, Aaron LaForge, Andrei Kamalov, Matthias F. Kling, Jonas Knurr, Ming-Fu Lin, Alberto A. Lutman, James P. MacArthur, Jon P. Marangos, Megan Nantel, Adi Natan, Razib Obaid, Jordan T. O'Neal, Niranjan H. Shivaram, Aviad Schori, Peter Walter, Anna Li Wang, Thomas J. A. Wolf, Agostino Marinelli, and James P. Cryan. Attosecond transient absorption spooktroscopy: a ghost imaging approach to ultrafast absorption spectroscopy. *Physical Chemistry Chemical Physics*, 22(5):2704–2712, February 2020. Publisher: The Royal Society of Chemistry.

[45] C. Guillot, Y. Ballu, J. Paigné, J. Lecante, K. P. Jain, P. Thiry, R. Pinchaux, Y. Pétroff, and L. M. Falicov. Resonant Photoemission in Nickel Metal. *Physical Review Letters*, 39(25):1632–1635, December 1977. Publisher: American Physical Society.

[46] P. Kolorenč and V. Averbukh. Fano-ADC(2,2) method for electronic decay rates. *The Journal of Chemical Physics*, 152(21):214107, June 2020.

[47] Marco Ruberti, Serguei Patchkovskii, and Vitali Averbukh. Quantum coherence in molecular photoionization. *Physical Chemistry Chemical Physics*, 24(33):19673–19686, 2022. Publisher: Royal Society of Chemistry.

[48] T. J. A. Wolf, R. H. Myhre, J. P. Cryan, S. Coriani, R. J. Squibb, A. Battistoni, N. Berrah, C. Bostedt, P. Bucksbaum, G. Coslovich, R. Feifel, K. J. Gaffney, J. Grilj, T. J. Martinez, S. Miyabe, S. P. Moeller, M. Mucke, A. Natan, R. Obaid, T. Osipov, O. Plekan, S. Wang, H. Koch, and M. Gühr. Probing ultrafast $\pi\pi^*$/nπ^* internal conversion in organic chromophores via K-edge resonant absorption. *Nature Communications*, 8(1):29, June 2017. Number: 1 Publisher: Nature Publishing Group.

[49] Federico Vismarra, Francisco Fernández-Villoria, Daniele Mocci, Jesús González-Vázquez, Yingxuan Wu, Lorenzo Colaizzi, Fabian Holzmeier, Jorge Delgado, José Santos, Luis Bañares, Laura Carlini, Mattea Carmen Castrovilli, Paola Bolognesi, Robert Richter, Lorenzo Avaldi, Alicia Palacios, Matteo Lucchini, Maurizio Reduzzi, Rocío Borrego-Varillas, Nazario Martín,

Fernando Martín, and Mauro Nisoli. Few-femtosecond electron transfer dynamics in photoionized donor–π–acceptor molecules. *Nature Chemistry*, pages 1–8, September 2024. Publisher: Nature Publishing Group.

[50] Morgane Vacher, Michael J. Bearpark, Michael A. Robb, and João Pedro Malhado. Electron Dynamics upon Ionization of Polyatomic Molecules: Coupling to Quantum Nuclear Motion and Decoherence. *Physical Review Letters*, 118(8):083001, February 2017.

[51] Zhen Zhang, Joseph Duris, James P. MacArthur, Alexander Zholents, Zhirong Huang, and Agostino Marinelli. Experimental demonstration of enhanced self-amplified spontaneous emission by photocathode temporal shaping and self-compression in a magnetic wiggler. *New Journal of Physics*, 22(8):083030, August 2020. Publisher: IOP Publishing.

[52] A. A. Lutman, R. Coffee, Y. Ding, Z. Huang, J. Krzywinski, T. Maxwell, M. Messerschmidt, and H.-D. Nuhn. Experimental Demonstration of Femtosecond Two-Color X-Ray Free-Electron Lasers. *Physical Review Letters*, 110(13):134801, March 2013.

[53] P. Walter, T. Osipov, M.-F. Lin, J. Cryan, T. Driver, A. Kamalov, A. Marinelli, J. Robinson, M. H. Seaberg, T. J. A. Wolf, J. Aldrich, N. Brown, E. G. Champenois, X. Cheng, D. Cocco, A. Conder, I. Curiel, A. Egger, J. M. Glownia, P. Heimann, M. Holmes, T. Johnson, L. Lee, X. Li, S. Moeller, D. S. Morton, M. L. Ng, K. Ninh, J. T. O'Neal, R. Obaid, A. Pai, W. Schlotter, J. Shepard, N. Shivaram, P. Stefan, X. Van, A. L. Wang, H. Wang, J. Yin, S. Yunus, D. Fritz, J. James, and J.-C. Castagna. The time-resolved atomic, molecular and optical science instrument at the Linac Coherent Light Source. *Journal of Synchrotron Radiation*, 29(4):957–968, July 2022. Number: 4 Publisher: International Union of Crystallography.

[54] Matthew Seaberg, Lance Lee, Daniel Morton, Xinxin Cheng, James Cryan, Gregorio Ivan Curiel, Brendan Dix, Taran Driver, Kay Fox, Corey Hardin, Andrei Kamalov, Kenan Li, Xiang Li, Ming-Fu Lin, Yanwei Liu, Tim Montagne, Razib Obaid, Anne Sakdinawat, Peter Stefan, Randy Whitney, Thomas Wolf, Lin Zhang, David Fritz, Peter Walter, Daniele Cocco, and May Ling Ng. The X-ray Focusing System at the Time-Resolved AMO Instrument. *Synchrotron Radiation News*, 35(2):20–28, March 2022. Publisher: Taylor & Francis _eprint: https://doi.org/10.1080/08940886.2022.2066416.

[55] Marco Ruberti. Restricted correlation space b-spline adc approach to molecular ionization: Theory and applications to total photoionization cross-sections. *Journal of Chemical Theory and Computation*, 15(6):3635–3653, 2019.

[56] Giovanni Li Manni, Ignacio Fdez. Galván, Ali Alavi, Flavia Aleotti, Francesco Aquilante, Jochen Autschbach, Davide Avagliano, Alberto Baiardi, Jie J. Bao, Stefano Battaglia, Letitia Birnoschi, Alejandro Blanco-González, Sergey I. Bokarev, Ria Broer, Roberto Cacciari, Paul B. Calio, Rebecca K. Carlson, Rafael Carvalho Couto, Luis Cerdán, Liviu F. Chibotaru, Nicholas F. Chilton, Jonathan Richard Church, Irene Conti, Sonia Coriani, Juliana Cuéllar-Zuquin, Razan E. Daoud, Nike Dattani, Piero Decleva, Coen De Graaf, Mickaël G. Delcey, Luca De Vico, Werner Dobrautz, Sijia S. Dong, Rulin Feng, Nicolas Ferré, Michael Filatov(Gulak), Laura Gagliardi, Marco Garavelli, Leticia González, Yafu Guan, Meiyuan Guo, Matthew R. Hennefarth, Matthew R. Hermes, Chad E. Hoyer, Miquel Huix-Rotllant, Vishal Kumar Jaiswal, Andy Kaiser, Danil S. Kaliakin, Marjan Khamesian, Daniel S. King, Vladislav Kochetov, Marek Krośnicki, Arpit Arun Kumaar, Ernst D. Larsson, Susi Lehtola, Marie-Bernadette Lepetit, Hans Lischka, Pablo López Ríos, Marcus Lundberg, Dongxia Ma, Sebastian Mai, Philipp Marquetand, Isabella C. D. Merritt, Francesco Montorsi, Maximilian Mörchen, Artur Nenov, Vu Ha Anh Nguyen, Yoshio Nishimoto, Meagan S. Oakley, Massimo Olivucci, Markus Oppel, Daniele Padula, Riddhish Pandharkar, Quan Manh Phung, Felix Plasser, Gerardo Raggi, Elisa Rebolini, Markus Reiher, Ivan Rivalta, Daniel Roca-Sanjuán, Thies Romig, Arta Anushirwan Safari, Aitor Sánchez-Mansilla, Andrew M. Sand, Igor Schapiro, Thais R. Scott, Javier Segarra-Martí, Francesco Segatta, Dumitru-Claudiu Sergentu, Prachi Sharma, Ron Shepard, Yinan Shu, Jakob K. Staab, Tjerk P. Straatsma, Lasse Kragh Sørensen, Bruno Nunes Cabral Tenorio, Donald G. Truhlar, Liviu Ungur, Morgane Vacher, Valera Veryazov, Torben Arne Voß, Oskar Weser, Dihua Wu, Xuchun Yang, David Yarkony, Chen Zhou, J. Patrick Zobel, and Roland Lindh. The OpenMolcas *Web* : A Community-Driven Approach to Advancing Computational Chemistry. *Journal of Chemical Theory and Computation*, 19(20):6933–6991, October 2023.

[57] Piero Decleva, Mauro Stener, and Daniele Toffoli. Continuum Electronic States: The Tiresia Code. *Molecules*, 27(6):2026, March 2022.

[58] D Toffoli, M Stener, G Fronzoni, and P Decleva. Convergence of the multicenter B-spline DFT approach for the continuum. *Chem. Phys.*, 276(1):25–43, January 2002.

[59] Aurora Ponzi, Marin Sapunar, Celestino Angeli, Renzo Cimiraglia, Nađa Došlić, and Piero Decleva. Photoionization of furan from the ground and excited electronic states. *The Journal of Chemical Physics*, 144(8):084307, February 2016.

[60] H Bachau, E Cormier, P Decleva, J E Hansen, and F Martín. Applications of *B*-splines in atomic and molecular physics. *Rep. Prog. Phys.*, 64(12):1815–1943, December 2001.

[61] Daniele Toffoli, Sonia Coriani, Mauro Stener, and Piero Decleva. Tiresia: A code for molecular electronic continuum states and photoionization. *Computer Physics Communications*, 297:109038, April 2024.

[62] Aurora Ponzi, Celestino Angeli, Renzo Cimiraglia, Sonia Coriani, and Piero Decleva. Dynamical photoionization observables of the CS molecule: The role of electron correlation. *The Journal of Chemical Physics*, 140(20):204304, May 2014.

[63] Torsha Moitra, Sonia Coriani, and Piero Decleva. Capturing Correlation Effects on Photoionization Dynamics. *Journal of Chemical Theory and Computation*, 17(8):5064–5079, August 2021.

[64] Jorge Delgado, Manuel Lara-Astiaso, Jesús González-Vázquez, Piero Decleva, Alicia Palacios, and Fernando Martín. Molecular fragmentation as a way to reveal early electron dynamics induced by attosecond pulses. *Faraday Discussions*, 228:349–377, 2021.

[65] Bruno Nunes Cabral Tenorio, Aurora Ponzi, Sonia Coriani, and Piero Decleva. Photoionization Observables from Multi-Reference Dyson Orbitals Coupled to B-Spline DFT and TD-DFT Continuum. *Molecules*, 27(4):1203, February 2022.

[66] F. Calegari, D. Ayuso, A. Trabattoni, L. Belshaw, S. De Camillis, S. Anumula, F. Frassetto, L. Poletto, A. Palacios, P. Decleva, J. B. Greenwood, F. Martín, and M. Nisoli. Ultrafast electron dynamics in phenylalanine initiated by attosecond pulses. *Science*, 346(6207):336–339, 2014.

[67] Manuel Lara-Astiaso, David Ayuso, Ivano Tavernelli, Piero Decleva, Alicia Palacios, and Fernando Martín. Decoherence, control and attosecond probing of XUV-induced charge migration in biomolecules. A theoretical outlook. *Faraday Discussions*, 194:41–59, 2016.

[68] Gilbert Grell, Zhaoheng Guo, Taran Driver, Piero Decleva, Etienne Plésiat, Antonio Picón, Jesús González-Vázquez, Peter Walter, Jonathan P. Marangos, James P. Cryan, Agostino Marinelli, Alicia Palacios, and Fernando Martín. Effect of the shot-to-shot variation on charge migration induced by sub-fs x-ray free-electron laser pulses. *Physical Review Research*, 5:023092, 2023.

[69] Raimund Feifel, John H. D. Eland, Richard J. Squibb, Melanie Mucke, Sergey Zagorodskikh, Per Linusson, Francesco Tarantelli, Přemysl Kolorenč, and Vitali Averbukh. Ultrafast Molecular Three-Electron Auger Decay. *Physical Review Letters*, 116(7):073001, February 2016.

[70] M. J. Frisch, G. W. Trucks, H. B. Schlegel, G. E. Scuseria, M. A. Robb, J. R. Cheeseman, G. Scalmani, V. Barone, G. A. Petersson, H. Nakatsuji, X. Li, M. Caricato, A. V. Marenich, J. Bloino, B. G. Janesko, R. Gomperts, B. Mennucci, H. P. Hratchian, J. V. Ortiz, A. F. Izmaylov, J. L. Sonnenberg, D. Williams-Young, F. Ding, F. Lipparini, F. Egidi, J. Goings, B. Peng, A. Petrone, T. Henderson, D. Ranasinghe, V. G. Zakrzewski, J. Gao, N. Rega, G. Zheng, W. Liang, M. Hada, M. Ehara, K. Toyota, R. Fukuda, J. Hasegawa, M. Ishida, T. Nakajima, Y. Honda, O. Kitao, H. Nakai, T. Vreven, K. Throssell, J. A. Montgomery, Jr., J. E. Peralta, F. Ogliaro, M. J. Bearpark, J. J. Heyd, E. N. Brothers, K. N. Kudin, V. N. Staroverov, T. A. Keith, R. Kobayashi, J. Normand, K. Raghavachari, A. P. Rendell, J. C. Burant, S. S. Iyengar, J. Tomasi, M. Cossi, J. M. Millam, M. Klene, C. Adamo, R. Cammi, J. W. Ochterski, R. L. Martin, K. Morokuma, O. Farkas, J. B. Foresman, and D. J. Fox. Gaussian 16 Revision E.01. Gaussian Inc., Wallingford CT, 2016.

[71] Mickael G. Delcey, Lasse Kragh Sørensen, Morgane Vacher, Rafael C. Couto, and Marcus Lundberg. Efficient calculations of a large number of highly excited states for multiconfigurational wavefunctions. *Journal of Computational Chemistry*, 40:1789–1799, April 2019.

[72] Per Åke Malmqvist, Kristine Pierloot, Abdul Rehaman Moughal Shahi, Christopher J. Cramer, and Laura Gagliardi. The restricted active space followed by second-order perturbation theory method: Theory and application to the study of CuO_2 and Cu_2O_2 systems. *The Journal of Chemical Physics*, 128(20):204109, 2008.

[73] Erik Källman, Mickaël G. Delcey, Meiyuan Guo, Roland Lindh, and Marcus Lundberg. Quantifying similarity for spectra with a large number of overlapping transitions: Examples from soft X-ray spectroscopy. *Chemical Physics*, 535:110786, July 2020.

[74] Eetu Pelimanni, Adam E. A. Fouda, Phay J. Ho, Thomas M. Baumann, Sergey I. Bokarev, Alberto De Fanis, Simon Dold, Gilbert Grell, Iyas Ismail, Dimitrios Koulentianos, Tommaso Mazza, Michael Meyer, Maria-Novella Piancastelli, Ralph Püttner, Daniel E. Rivas, Björn Senfftleben, Marc Simon, Linda Young, and Gilles Doumy. Observation of molecular resonant double-core excitation driven by intense X-ray pulses. *Communications Physics*, 7(1):341, October 2024.

[75] Nina Ignatova, Victor Kimberg, Faris Gel'mukhanov, Annette Pietzsch, Sebastian Eckert, Mattis Fondell, Brian Kennedy, Marcus Dantz, Thorsten Schmitt, Michael Odelius, Alexander Föhlisch, and Vinícius Vaz Da Cruz. Ballistic and delayed photodissociation channels in the $B\tilde{2}$ A 1 1 state of water studied with resonant inelastic x-ray scattering. *Physical Review A*, 110(3):033119, September 2024.

[76] Gilbert Grell and Sergey I. Bokarev. Multi-reference protocol for (auto)ionization spectra: Application to molecules. *The Journal of Chemical Physics*, 152(7):074108, February 2020.

[77] Gilbert Grell, Vladislav Kochetov, Tobias Marx, Andy Kaiser, and Sergey I. Bokarev. SCAMPI - Spherical Continuum for Auger-Meitner Decay and Photoionization. Code available by contacting the authors, 2016-2024.

[78] Per Åke Malmqvist, Björn O. Roos, and Bernd Schimmelpfennig. The restricted active space (RAS) state interaction approach with spin–orbit coupling. *Chemical Physics Letters*, 357(3-4):230–240, May 2002.

[79] G. te Velde, F. M. Bickelhaupt, E. J. Baerends, C. Fonseca Guerra, S. J. A. van Gisbergen, J. G. Snijders, and T. Ziegler. Chemistry with ADF. *J. Comput. Chem.*, 22(9):931–967, July 2001.

[80] Charlotte Froese Fischer and Muhammad Idrees. Spline algorithms for continuum functions. *Computers in Physics*, 3(3):53, 1989.

[81] M. Brosolo and P. Decleva. Variational approach to continuum orbitals in a spline basis: An application to H2+ photoionization. *Chemical Physics*, 159(2):185–196, January 1992.

[82] M. Ruberti. Quantum electronic coherences by attosecond transient absorption spectroscopy: ab initio B-spline RCS-ADC study. *Faraday Discuss.*, 228(0):286–311, 2021.

[83] M. Ruberti and V. Averbukh. Advances in modeling attosecond electron dynamics in molecular photoionization. *WIREs Comput. Mol. Sci.*, 13:e1673, 2023.

[84] E.R. Simpson, A. Sanchez-Gonzalez, D.R. Austin, Z. Diveki, S.E.E. Hutchinson, T. Siegel, M. Ruberti, V. Averbukh, L. Miseikis, C.S. Struber, L. Chipperfield, and J.P. Marangos. Polarisation response of delay dependent absorption modulation in strong field dressed helium atoms probed near threshold. *New J. Phys.*, 18:083032, 2016.

[85] D. You, K. Ueda, M. Ruberti, K.L. Ishikawa, P.A. Carpeggiani, T. Csizmadia, L. Gulyas, N.G. Harshitha, G. Sansone, P. Maroju, K. Kooser, C. Callegari, M. Di-Fraia, O. Plekan, R. Richter, L. Giannessi, E. Allaria, G. De Ninno, M. Trovo, L. Badano, B. Diviacco, D. Gauthier, N. Mirian, G. Penco, P. Rebernik, S. Spampinati, C. Spezzani, S. Di Mitri, G. Gaio, and K.C. Prince. A detailed investigation of single-photon laser enabled Auger decay in neon. *New J. Phys.*, 21:113036, 2019.

[86] M. Ruberti, P. Decleva, and V. Averbukh. Full Ab Initio Many-Electron Simulation of Attosecond Molecular Pump–Probe Spectroscopy. *Journal of Chemical Theory and Computation*, 14(10):4991–5000, October 2018. Publisher: American Chemical Society.

[87] M. Ruberti, P. Decleva, and V. Averbukh. Multi-channel dynamics in high harmonic generation of aligned CO_2: ab initio analysis with time-dependent B-spline algebraic diagrammatic construction. *Phys. Chem. Chem. Phys.*, 20(12):8311–8325, 2018.

[88] A.C. Bray, A. S. Maxwell, Y. Kissin, M. Ruberti, M. F. Ciappina, V. Averbukh, and C. Figueira De Morisson Faria. Polarization in strong-field ionization of excited helium. *J. Phys. B: Atomic, Molecular and Optical Physics*, 54:194002, 2021.

[89] Daniel Ratner, A Brachmann, FJ Decker, Y Ding, D Dowell, P Emma, A Fisher, J Frisch, S Gilevich, Z Huang, et al. Second and third harmonic measurements at the linac coherent light source. *Physical Review Special Topics—Accelerators and Beams*, 14(6):060701, 2011.

Acknowledgments

The authors gratefully acknowledge Jun Wang for expert support of the data analysis software.

Funding: Use of the Linac Coherent Light Source (LCLS), SLAC National Accelerator Laboratory, is supported by the U.S. Department of Energy (DOE), Office of Science, Office of Basic Energy Sciences (BES) under contract no. DE-AC02-76SF00515.

The work performed by T.D., E.I., J.T.O., D.G., E.T., A.L.W., T.J.A.W., M.F.K., P.H.B., and J.P.C. were supported by the Chemical Sciences, Geosciences, and Biosciences Division (CSGB), BES, DOE. Z.G., D.C., J.D., S.L., K.A.L., P.L.F. N.S.S., R.R., Z.Z., and A.M. acknowledge support from the Accelerator and Detector Research Program of the Department of Energy, Basic Energy Sciences division. The work by G.A.M, D.T., Z.W., and L.F.D was supported by CSGB, BES, DOE under award no. DE-FG02-04ER15614 and DE-SC0012462. S.B. and N.B. acknowledge support from CSGB, BES, DOE under award no. DE-SC0012376. K.B. was supported by the Chemical Sciences, Geosciences, and Biosciences Division, Office of Basic Energy Sciences, Office of Science, US Department of Energy, Grant No. DE-FG02-86ER13491 and acknowledges additional support by the US Department of Energy, Office of Science, Office of Workforce Development for Teachers and Scientists, Office of Science Graduate Student Research (SCGSR) program. The SCGSR program is administered by the Oak Ridge Institute for Science and Education (ORISE) for the DOE. ORISE is managed by ORAU under contract number DE-SC0014664. The work by G.G., A.Pa., and F.M. was funded through the European Research Council (ERC) under the European Union's Horizon 2020 research and innovation programme (grant agreement no. 951224, TOMATTO), the European COST Action CA18222 (AttoChem), supported by COST (European

Cooperation in Science and Technology), the Comunidad de Madrid (project FULMATEN, Ref. Y2018 NMT-5028), the Spanish Ministerio de Ciencia e Innovación (projects PID2022-138288NB-C31 and PID2022-138288NB-C32, the "Severo Ochoa" Programme for Centres of Excellence in R&D CEX2020-001039-S and the "María de Maeztu" Programme for Units of Excellence in R&D CEX2018-000805-M). The calculations labeled RAS-SXD were performed at the Mare Nostrum Supercomputer of the Red Española de Supercomputación (BSC-RES) and the Centro de Computación Científica de la Universidad Autónoma de Madrid (CCC-UAM). The work by M.R. and V.A. was supported by the EPSRC grant number EP/V009192/1. A.Pi. acknowledges the Spanish Ministry of Science, Innovation and Universities & the State Research Agency through grants refs. PID2021-126560NB-I00 and CNS2022-135803 (MCIU/AEI/FEDER, UE), and the "María de Maeztu" Programme for Units of Excellence in R&D (CEX2023-001316-M). K.B., E.W., D.R., and A.R. were supported by the U.S. DOE, Office of Science, Office of BES, CSGB under Award No. DE-FG02-86ER13491." The work by O.A. and J.P.M. was supported by UK EPSRC grants EP/X026094/1, EP/V026690/1 and EP/T006943/1 G.D and L.Y. were supported by the U.S. DOE, BES, CSGB under contract DE-AC02-06CH11357. Work by O.G., D.S.S., M.S. and T.W. was supported by DOE BES CSGB under Award No. DE-AC02-05CH11231.

Author contributions: T.D., P.H.B., M.F.K., J.P.M., P.W., A.M., J.P.C. conceived the research. T.D., Z.G., J.T.O., O.A., D.C., J.D., D.G., K.A.L., S.L., G.A.M., D.T., N.B., C.B., K.B., X.C., L.F.D., G.D., P.L.F., A.K., X.L., M.F.L., R.O., R.R.R., D.R., A.R., D.S.S., N.S.S., E.T., K.U., E.W., A.L.W., T.W., T.J.A.W., L.Y., Z.Z., O.G., M.F.K., J.P.M., P.W., A.M., J.P.C. participated in collecting the data. Z.G., D.C., J.D., S.L., P.L.F., R.R.R., N.S.S., Z.Z., A.M. generated the attosecond XFEL pulse pairs. E.I., T.D., Z.G., J.T.O., O.A., S.B., D.C., J.D., D.G., K.A.L., S.L., P.K., G.A.M., D.T., Z.W., J.P.C. performed data analysis. G.G., M.R., P.K., G.A.M., A.Pi., V.A., A.Pa., F.M. generated theoretical calculations. All authors participated in interpreting the results and writing the manuscript.

Competing interests: There are no competing interests to declare.

Data and materials availability: Data will be made publicly accessible when the paper is published.

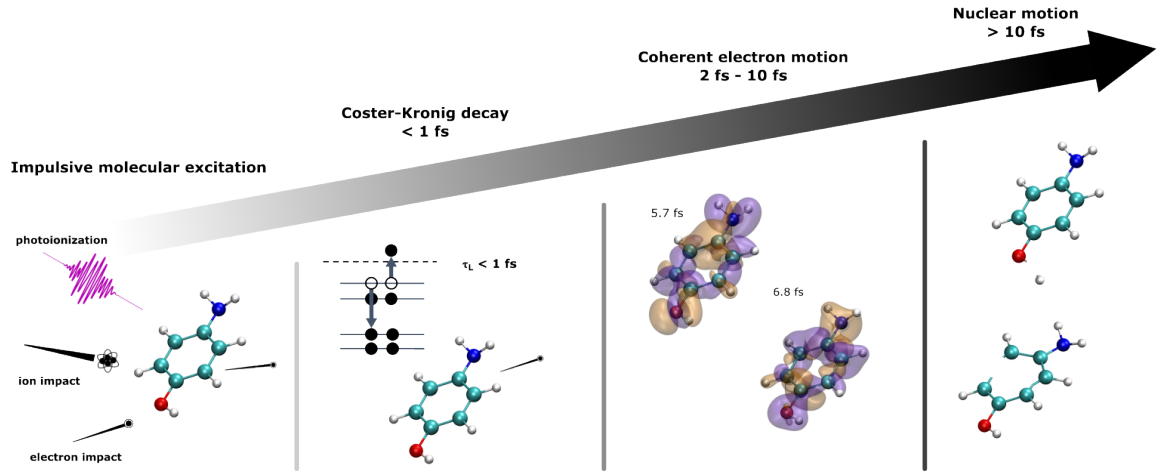

Figure 1: **Molecular response to impulsive ionization**. (left) Impulsive excitation can be driven by high-energy photons, ions, or electrons. The ultrafast molecular response evolves on multiple characteristic timescales: Coster-Kronig autoionization occurring within the first femtosecond, coherent electron motion lasting for several femtoseconds, and nuclear motion leading to the breaking and forming of chemical bonds after ~10 fs.

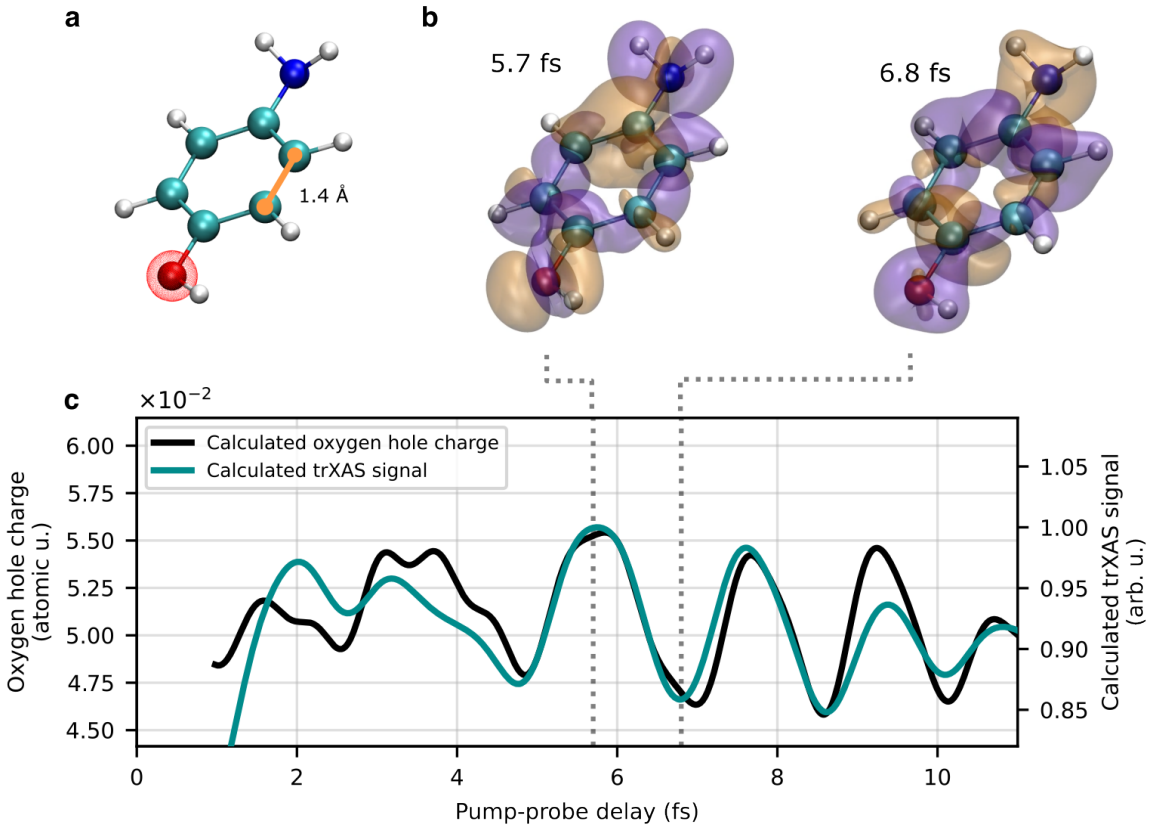

Figure 2: **Simulation of ultrafast charge motion in para-aminophenol probed by trXAS at the oxygen *K*-edge. a**, Molecular structure of para-aminophenol. Opaque spheres represent atomic positions: carbon (light blue), nitrogen (dark blue), oxygen (red), hydrogen (white). The translucent red sphere indicates the region of integration used to define the hole charge in panel **c**. **b**, Snapshots of the time-dependent part of the hole density ($\pm 1 \times 10^{-4}$ isosurface), calculated using the RAS-SXD method (see main text for details). The dynamics are calculated following ionization by a 3.7 eV bandwidth x-ray pulse centered at 260 eV. Purple represents a decrease in hole density (with respect to the static part of the hole density) and orange represents an increase. **c** Hole density in the vicinity of the oxygen atom (hole density integrated over the red translucent sphere in panel **a**) compared to the simulated oxygen *K*-edge XAS signal in the probe photon energy range from 523–529 eV, calculated *via* the RAS-SXD method (see main text).The close agreement between the two curves demonstrates that the cross-section for absorption at the oxygen site is proportional to hole charge at the oxygen site. Further, the curves start after the pump has decayed to zero, to minimize the influence of the incoherent cation population dynamics driven by the pump. To highlight the sensitivity of the trXAS to the coherent electron motion, autoionization by super Coster-Kronig decay has been excluded in this figure.

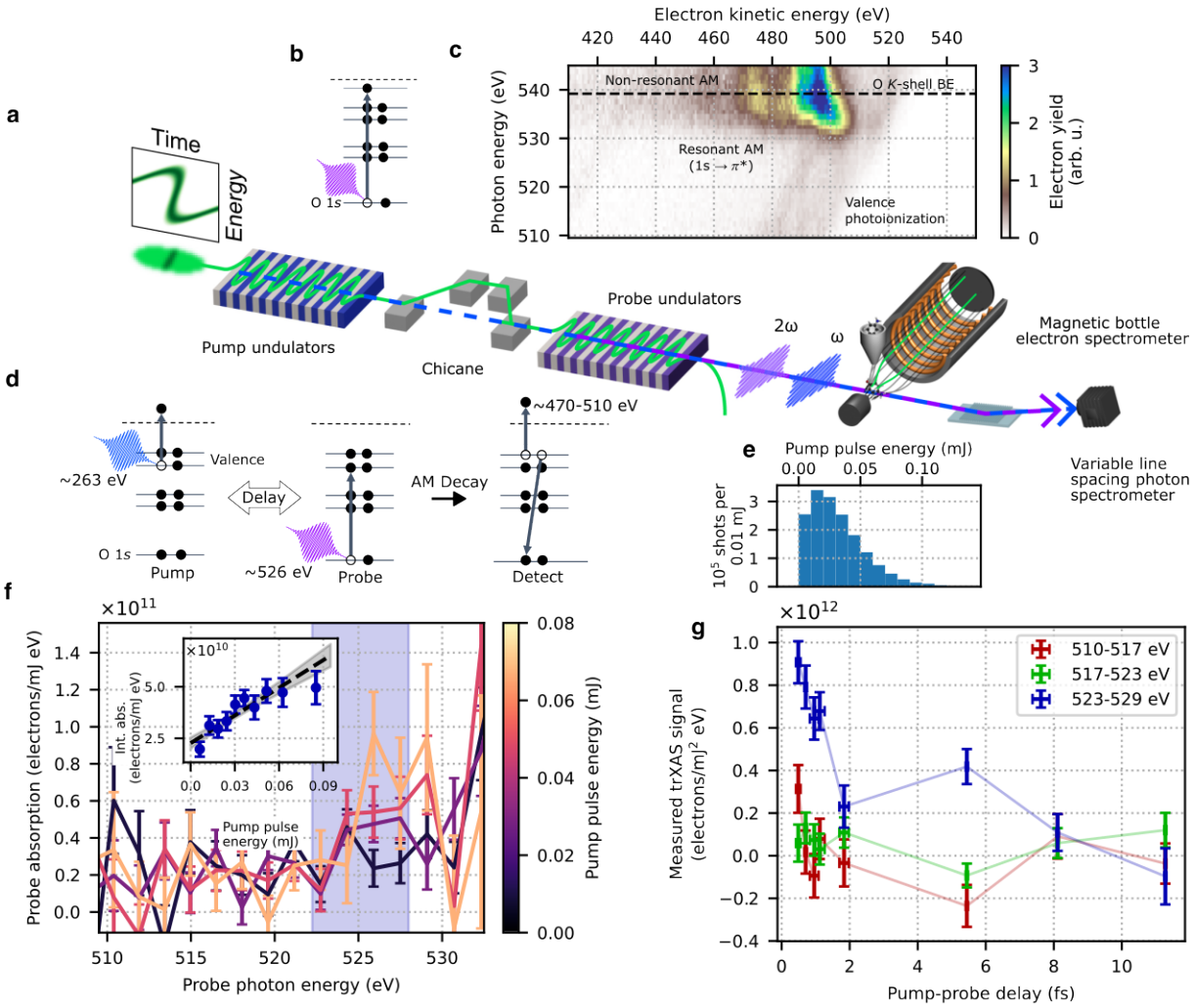

Figure 3: **a**, Experimental schematic showing the XFEL beamline, magnetic bottle electron spectrometer and x-ray spectrometer. **b**, Energy level diagram illustrating resonant x-ray absorption below the oxygen *K*-edge in the ground state molecule. **c**, Measured photon-energy resolved electron kinetic energy spectrum for the ground state molecule. The trXAS cross-section is calculated using the integrated electron yield in a kinetic energy range of 420–550 eV. **d**, Energy level diagram illustrating the pump, probe, and detection scheme used in this measurement. **e**, Distribution of pump pulse energies used in the experiment. **f**, Probe absorption as a function of probe photon energy (x-axis) and pump pulse energy (see colorbar), for a pump-probe delay of 5.4 fs. The inset shows the pump pulse energy dependence of the integrated yield in the blue shaded region. **g**, trXAS signal as a function of pump-probe delay for three different probe photon energy ranges.

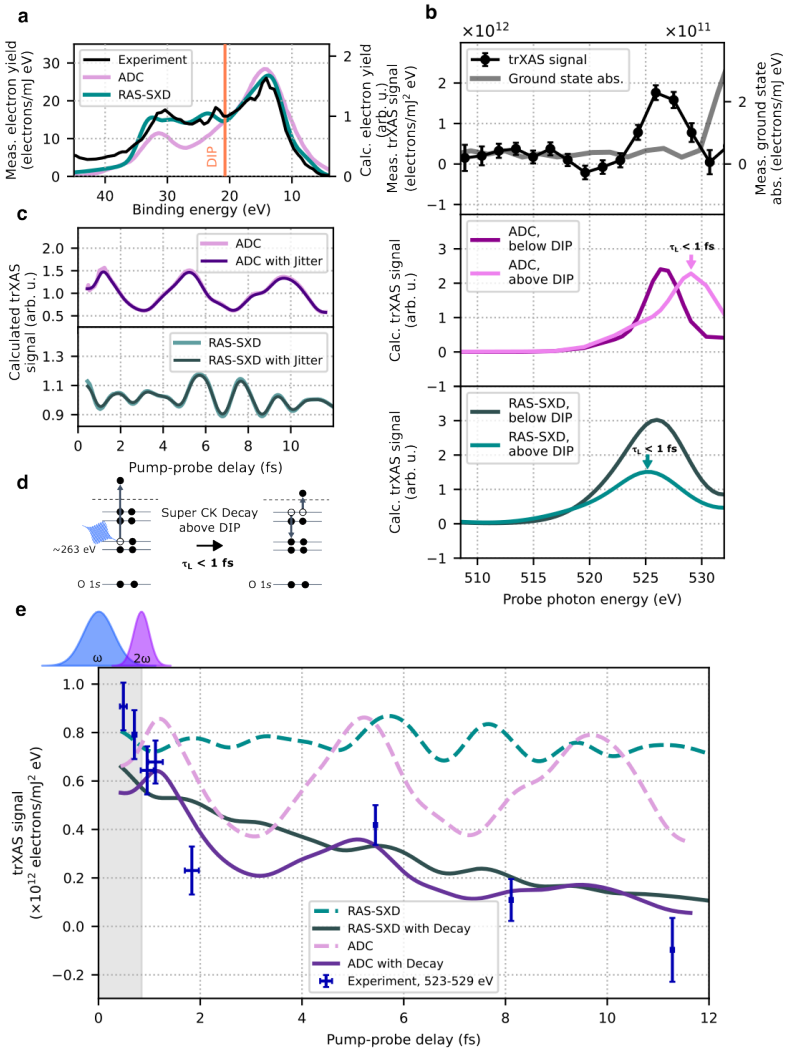

Figure 4: **a**, Simulated valence photoelectron spectrum produced by pump pulse compared to experimental results, where DIP is the double ionization potential (∼ 21 eV). **b**, Measured trXAS signal at 0.49 fs pump-probe delay (black line, upper panel) and ground-state absorption (gray line, upper panel), calculated ADC cation trXAS signal at 1.05 fs pump-probe delay (middle panel) and calculated RAS-SXD cation trXAS signal at 0.49 fs pump-probe delay (lower panel). The ground-state absorption overlaps with pump-probe signal (shown in gray) at higher photon energies (>530 eV). The calculated absorption signals are plotted separately for states above and below the DIP. As discussed in the text, the states above the DIP decay within less than 1 fs, as shown by the vertical arrows. **c**, Calculated trXAS signal integrated across the photon energy range 523-529 eV. **d**, Schematic showing the non-radiative super-Coster-Kronig decay process for cationic states above the DIP. **e**, Comparison between the calculated and measured trXAS signals. Solid lines incorporate a phenomenological decay term to account for nuclear motion (see text). The intensity profiles of the pump (blue) and probe (purple) pulses are shaded in the top left for a pump-probe delay of 0.85 fs.

Supplementary Information for Attosecond Coherent Electron Motion in a Photoionized Aromatic Molecule

Taran Driver et al.

1 Numerical Simulations

1.1 RAS-SXD Simulation Method

The 'RAS-SXD' abbreviation refers to the herein-employed combination of the restricted active space (RAS) quantum chemistry methods, to model multi-configurational bound states and O($1s$) absorption dipole moments of p-aminophenol, on the one hand, with the static-exchange B-spline density functional theory (SXD) method [60, 58] to evaluate the respective continuum orbitals and photoionization amplitudes, on the other hand. We use the OPENMOLCAS software [56] for the former, and the TIRESIA code implemented by Decleva et al. [57, 61] for the latter. Evaluating photoionization dipole moments in terms of SXD continuum orbitals and Dyson orbitals obtained from multi-reference bound-state quantum-chemistry methods has been introduced previously [62, 59] and by now has been applied to a wide range of molecular systems [62, 59, 63, 64, 65].

1.1.1 Pump Ionization and Hole-Charge Dynamics

The pump and probe pulses are modeled as Gaussian fields centered at their half duration $T/2$,

$$E(t) = E_0 \cos\left[\omega\,(t - T/2)\right] \mathrm{e}^{-\frac{(t-T/2)^2}{2\sigma^2}} \,. \tag{S1}$$

For the pump, we use a central frequency $\omega_1 = 260$ eV and an FWHM width of 0.70 fs, corresponding to a total duration of $T_1 = 1.96$ fs for $|E_1(t)|$, obtained from the 99.9% percentile ($\approx \pm 3.29\,\sigma_1$) of the envelope. The related FWHM-widths are 0.49 fs for $|E_1(t)|^2$, 5.2 eV for $|\tilde{E}_1(\omega)|$, and 3.7 eV for$|\tilde{E}_1(\omega)|^2$. We model the dynamics of the created electron hole in an extension of the previously introduced single-configurational approach [66, 67, 68]. In that, besides accounting

for multi-configurational bound states, the valence autoionization of cation states lying above the double-ionization potential (DIP) by Super Coster-Kronig Decay is taken into account. For smaller molecules, valence autoionization lifetimes in the range of 1 fs to few fs have been reported [69]. Herein, the autoionization life times of p-aminophenol cationic states above the DIP have been estimated with the Fano-ADC(2,2) method [46], see Supplemental Material section 1.2, as

$$\frac{1}{\Gamma_i} = \tau_i = \begin{cases} 0.345 \text{ fs}, & \text{DIP} \leq \mathcal{E}_{ig} < 23 \text{ eV} \\ 0.425 \text{ fs}, & 23 \text{ eV} \leq \mathcal{E}_{ig} < 30 \text{ eV} \\ 0.864 \text{ fs}, & 30 \text{ eV} \leq \mathcal{E}_{ig} < 34 \text{ eV} \end{cases}, \tag{S2}$$

suggesting a sub-fs time-scale for the cation autoionization.

Within the RAS-SXD approach, double-ionization potentials (DIPs) of 20.745 eV for the lowest lying singlet dication and of 21.96 eV for the lowest triplet dication states have been obtained at the RASPT2 level, defining the overall DIP to be 20.745 eV. Below the DIP lie 125 of the total 2226 included cation states, while the remaining states undergo valence autoionization, see computational details in Sect. 1.1.4. This is accounted for herein from the start of the pump interaction by incorporating a phenomenological decay into the expansion of the coherent superposition of cation states generated by the pump ionization,

$$\left|\Psi^+(t)\right\rangle = \sum_{i=1}^{N^+_{\text{val}}} \sum_L \int d\varepsilon \, C^+_{i,L}(t,\varepsilon) \mathrm{e}^{-[\mathrm{i}(\mathcal{E}_i+\varepsilon)+\frac{\Gamma_i}{2}]t} \left|\Psi^+_{i,L}(\varepsilon)\right\rangle, \tag{S3}$$

ensuring that the population of the cation states above the DIP decays with $\propto \mathrm{e}^{-\Gamma_i t}$, while $\Gamma_i = 0$ for the states below the DIP. $|\Psi^+_{i,L}(\varepsilon)\rangle$ denotes the single-channel continuum state constructed by the linear combination,

$$\left|\Psi^+_{i,L}(\varepsilon)\right\rangle = \frac{1}{\sqrt{2}} \left[\boldsymbol{a}^\dagger_{L,-\frac{1}{2}}(\varepsilon) \left|\Psi_i^{+,\frac{1}{2}}\right\rangle - \boldsymbol{a}^\dagger_{L,\frac{1}{2}}(\varepsilon) \left|\Psi_i^{+,-\frac{1}{2}}\right\rangle \right], \tag{S4}$$

conserving the singlet spin of the neutral ground state. The operation $\boldsymbol{a}^\dagger_{L,\sigma}(\varepsilon)\left|\Psi_i^{+,M_+}\right\rangle$ inserts and antisymmetrizes a continuum orbital with asymptotic kinetic energy ε, angular momentum and magnetic quantum number $L = (l, m)$ and spin projection $\sigma \in \{-\frac{1}{2}, \frac{1}{2}\}$ into the ith bound (doublet) cation state with spin projection $M^+ \in \{-\frac{1}{2}, \frac{1}{2}\}$.

The photoionization amplitudes are obtained in first order of time-dependent perturbation theory as

$$C^{+}_{i,L}(t,\varepsilon,\boldsymbol{u}_1) = \mathrm{i}\boldsymbol{\mu}_{ig,L}(\varepsilon)\cdot\boldsymbol{u}_1\int_0^t E_1(t')\mathrm{e}^{\frac{\Gamma_i}{2}t'}\mathrm{e}^{\mathrm{i}(\mathcal{E}_{ig}+\varepsilon)t'}dt', \tag{S5}$$

where $E_1(t)$ is the probe-field centered at $t = T_1/2$, with polarization vector $\boldsymbol{u}_1$. During the pulse, $t < T_1$, the integral is evaluated numerically, while a closed form can be given for fields of the form of Eq. (S1) in terms of their Fourier transform, $\tilde{E}_1(\omega) = \mathcal{F}[E_1(t)](\omega)$, at the instant when the pump pulse has decayed to zero, $t = T_1$,

$$C^{+}_{i,L}(T_1,\varepsilon,\boldsymbol{u}_1) = \mathrm{i}\sqrt{2\pi}\boldsymbol{\mu}_{ig,L}(\varepsilon)\cdot\boldsymbol{u}_1\tilde{E}_1^{*}(\mathcal{E}_{ig}+\varepsilon)\mathrm{e}^{\frac{\Gamma_i^2\sigma_1^2}{8}}\mathrm{e}^{\frac{\Gamma_i T_1}{4}}\mathrm{e}^{\mathrm{i}(\mathcal{E}_{ig}+\varepsilon-\omega_1)\frac{\Gamma_i\sigma_1^2}{2}}. \tag{S6}$$

The photoionization dipoles, $\boldsymbol{\mu}_{ig,L}(\varepsilon)$, are obtained between the spatial continuum orbital, $|\phi_L(\varepsilon)\rangle$, and spatial Dyson orbital, $|\Phi_{ig}\rangle$, of the neutral ground state, $|\Psi_g\rangle$, and the ith bound cation state, $|\Psi_i^{+,\frac{1}{2}}\rangle$,

$$\boldsymbol{\mu}_{ig,L}(\varepsilon) = \sqrt{2}\left\langle\phi_L(\varepsilon)\,\middle|\,\boldsymbol{r}\,\middle|\,\Phi_{ig}\right\rangle. \tag{S7}$$

The prefactor of $\sqrt{2}$ is a result of accounting for the different combinations of the cation bound and continuum orbital spin projections introduced in Eq. (S4).

To allow for a computationally tractable electronic propagation and evaluation of the probe step, the continuum character is traced out, which yields a quantum mixture of bound cationic states, defined for the pump pulse polarized along the $\alpha = x, y, z$ directions by the density matrices,

$$\gamma^{+}_{ij,\alpha}(t) = \sum_L\int d\varepsilon\, C^{+}_{i,L}(t,\varepsilon,\boldsymbol{e}_\alpha)\left(C^{+}_{j,L}(t,\varepsilon,\boldsymbol{e}_\alpha)\right)^{*}\mathrm{e}^{-\frac{\Gamma_i+\Gamma_j}{2}t}, \tag{S8}$$

into which the autoionization decay between $0 \le t' \le t$ has been included as well. The free evolution

of the mixed cation state populated by the pump is then expressed as, dropping spin indices,

$$\boldsymbol{\rho}_{\alpha}^{+}(t') = \sum_{ij} \rho_{ij,\alpha}^{+}(t') |\Psi_i^+\rangle\langle\Psi_j^+| \mathrm{e}^{-\mathrm{i}\mathcal{E}_{ij}t'} , \tag{S9}$$

$$\rho_{ij,\alpha}^{+}(t') = \begin{cases} \gamma_{ij,\alpha}^{+}(t'), & t' < T_1 \\ \gamma_{ij,\alpha}^{+}(T_1) \exp -\frac{\Gamma_i+\Gamma_j}{2} t, & t' = T_1 + t \end{cases} . \tag{S10}$$

Note that the second line of Eq. (S10), i.e. for times $t' = T_1 + t$, separates the autoionization decay from the density matrix $\gamma_{ij,\alpha}^{+}(T_1)$, which allows in the following to decouple the double integral for the pump-probe trXAS spectral expression, in Eq. S13. Tracing out the continuum is justified by the high kinetic energies of over 200 eV, due to which the continuum electrons leave the molecular region very fast. In order to obtain a tractable expression for the trXAS in presence of the pump pulse, approximate cation density matrices are obtained in the same way on a temporal grid for the duration of the pump pulse, $t' < T_1$. This corresponds to the approximation that the electrons leave the system instantly during the presence of the pulse.

The dynamic portion of the cation hole density created by the pump, reflecting the off-diagonal matrix elements, i.e., the electronic coherence, which is shown in Figs. 1 & 2b is obtained as,

$$\rho_{\mathrm{hole}}^{\mathrm{dyn}}(\boldsymbol{r}, T_1 + t) = -\sum_{i \neq j} \gamma_{ij}^{+,\mathrm{noAI}}(T_1) \sum_{pq} \rho_{ji;pq}^{1e} \, \phi_p(\boldsymbol{r}) \phi_q(\boldsymbol{r}) \mathrm{e}^{-\mathrm{i}\mathcal{E}_{ij}(T_1+t)} . \tag{S11}$$

As the evaluation of the 3D spatial densities is considerably simplified if the density matrix is constant, autoionization of the cation states above the DIP has been switched off by using $\gamma_{ij,\alpha}^{+,\mathrm{noAI}}(T_1)$, where all $\Gamma_i = 0$, and the data is shown for delays $\tau > \frac{T_1}{2}$, where the pump has already decayed to zero. The average over molecular orientations has been taken into account by using $\gamma_{ij}^{+,\mathrm{noAI}}(T_1) = \frac{1}{3} \sum_{\alpha=x,y,z} \gamma_{ij,\alpha}^{+,\mathrm{noAI}}(T_1)$. The dynamic hole density is connected to the cation molecular orbitals $\phi_p(\boldsymbol{r})$, $\phi_q(\boldsymbol{r})$ by means of the spin-summed one-electron transition density matrix $\rho_{ji;pq}^{1e}$. The oscillation frequencies are the cationic energy differences $\mathcal{E}_{ij}$. The localized dynamic hole charge plotted in Fig. 2c has been obtained by integrating the dynamic hole-density in Eq. (S11) over a sphere with $r = 1.0$ a.u. centered on the oxygen atom of p-aminophenol, indicated in Fig. 2a.

1.1.2 Transient Pump-Probe XAS Signal

The O(1s) transient XAS (trXAS) is evaluated by solving the von Neumann equation for the time evolution of the mixed cationic state defined in Eq. (S9) in presence of the probe pulse, $E_2(t)$, with duration T_2 to second-order of time-dependent perturbation theory. For a probe-pulse arrival time t' one has,

$$\begin{aligned} P^{\mathrm{trXAS}}_{\mathrm{O}(1s)}(t', E_2) =& \frac{2}{3} \sum_{f}^{N^+_{\mathrm{O}(1s)}} \sum_{i,j}^{N^+_{\mathrm{val}}} \sum_{\alpha=x,y,z} \mu_{fi,\alpha}\mu_{jf,\alpha} \int_0^{T_2} dt_2 E_2(t_2) \int_0^{t_2} dt_1 E_2(t_1) \\ & \times \mathbf{Re}\left[\rho^+_{ij,\alpha}(t'+t_1)\mathrm{e}^{-\mathrm{i}\mathcal{E}_{fj}(t'+t_1)}\mathrm{e}^{-\mathrm{i}\mathcal{E}_{if}(t'+t_2)}\right] . \end{aligned} \tag{S12}$$

Defining the probe pulse analogously to the pump pulse, Eq. (S1), $t' = 0$ indicates that the rising flanks of pump and probe pulses arrive at the same time, while their maxima arrive at $\frac{T_1}{2}$ and $\frac{T_2}{2}$, respectively. $\mu_{fi,\alpha}$ is the α component of the, in this case real, O(1s) absorption transition dipole moment between cation valence state i and O(1s)-hole state f; $\mathcal{E}_{fi}$ denotes the respective energy difference absorbed from the probe field. Note that the autoionization decay is included in the definition of $\rho^+_{ij,\alpha}(t)$, Eq. (S10). Probe pulses with a spectral FWHM of 5.0 eV of $|\tilde{E}_2(\omega)|^2$, corresponding to FWHM durations of 0.37 fs for $|E_2(t)|^2$ and 0.52 fs for $|E_2(t)|$ with a total duration of T_2=1.44 fs have been used. Since pump and probe pulses share the same polarization, the average over molecular orientations has been accounted for by averaging over the $x-x$, $y-y$, and $z-z$ combinations of pump and probe dipole components.

The double-integral in Eq. (S12) is evaluated numerically for probe arrival times $t' < T_1$, i.e., if the pulses overlap. If the probe pulse arrives after the pump has decayed, at $t' = T_1 + t$, the double integral can be decoupled and the following expression is found,

$$\begin{aligned} P^{\mathrm{trXAS}}_{\mathrm{O}(1s)}(T_1+t, E_2) =& \frac{2\pi}{3} \sum_{f}^{N^+_{\mathrm{O}(1s)}} \sum_{i,j}^{N^+_{\mathrm{val}}} \sum_{\alpha=x,y,z} \gamma^+_{ij,\alpha}(T_1)\mathrm{e}^{-[\mathrm{i}\mathcal{E}_{ij}(T_1+t)+\frac{1}{2}(\Gamma_i+\Gamma_j)t]}\mu_{fi,\alpha}\mu_{jf,\alpha} \\ & \times \mathcal{F}\left[E_2(t)\mathrm{e}^{-\frac{\Gamma_i}{2}t}\right]^*(\mathcal{E}_{fi})\mathcal{F}\left[E_2(t)\mathrm{e}^{-\frac{\Gamma_j}{2}t}\right](\mathcal{E}_{fj}) \end{aligned} , \tag{S13}$$

with $\mathcal{F}[\,\cdot\,]$ denoting the Fourier transformation and t representing the field-free time between pulses. It is related to the pump-probe delay between the pulse maxima as $\tau = t + \frac{T_1+T_2}{2}$. Facilitating

the expressions in Eq. (S12), to describe the region where pump and probe pulses overlap and Eq. (S13) to describe the region of non-overlapping pulses, gives access to the trXAS starting from a minimal delay of $\tau_{\min} = \frac{T_2 - T_1}{2}$, corresponding to $\tau_{\min} = -0.26$ fs for the present pulse durations. The trXAS has been obtained for central probe energies from 505 eV to 555 eV for delays between $\tau_{\min}$ and 12 fs. To obtain the time-dependent curves, the trXAS has been integrated over the peak between 523 eV and 529 eV, enclosing the absorption feature below 530 eV that has been measured in the experiment, see Fig. S6.

1.1.3 Dication Population Dynamics and trXAS

Including the 362 (166 singlet and 196 triplet) dication states below 35 eV of ionization energy to keep the computational costs under control, the cation-dication autoionization population dynamics is modeled by a master equation driven by the Fano-ADC(2,2) decay rates, given in Eq. (S2), $\dot{\rho}^{2+}_{aa,\alpha}(t) = \sum_i \Gamma_{i,a} \rho^{+}_{ii,\alpha}(t)$, which has the solution,

$$\rho^{2+}_{aa,\alpha}(t') = \begin{cases} \sum_i [\rho^{+,\mathrm{noAI}}_{ii,\alpha}(t') - \rho^{+}_{ii,\alpha}(t')] \frac{\Gamma_{i,a}}{\Gamma_i}, & t' \leq T_1 \\ \rho^{2+}_{aa,\alpha}(T_1) + \sum_i \frac{\Gamma_{i,a}}{\Gamma_i} \rho^{+}_{ii,\alpha}(T_1) \left(1 - \mathrm{e}^{-\Gamma_i t}\right), & t' = T_1 + t \end{cases} . \tag{S14}$$

Note that dication populations created during the pump-pulse, $t' \leq T_1$ are obtained from the difference of the cation populations with, $\rho^{+}_{ii}(t')$, and without autoionization, $\rho^{+,\mathrm{noAI}}_{ii}(t')$, ensuring the conservation of the total norm. Assuming equal probabilities of all (singlet and triplet) open dication energies, the partial decay rates are estimated in terms of the total decay rate multiplied with the ratio of the energy interval occupied by the dication state a, $\Delta\mathcal{E}^{2+}_a$, and the total range of open dication state energies,

$$\Gamma_{i,a} = \Gamma_i \cdot \frac{\Delta\mathcal{E}^{2+}_a}{\sum_{b;\mathcal{E}^{2+}_b < \mathcal{E}^{+}_i} \Delta\mathcal{E}^{+}_b} . \tag{S15}$$

The dication trXAS is then obtained in the same manner as for the cation, using Eq. (S12) for the region of overlapping pulses and Eq. (S13) for larger pump-probe delays. However, only the dication populations defined by Eq. (S14), i.e. the diagonal of the density matrix, can be taken into account at this level of theory.

1.1.4 Computational Details

RAS Bound State Calculations The equilibrium geometry has been optimized with the GAUSSIAN16 program [70] at the DFT level using the B3LYP functional and *cc-pVTZ* basis set. The neutral, cationic, and dicationic bound states have been computed with the restricted active space self-consistent field (RASSCF) method in OPENMOLCAS [56] using the *ANO-L TZP* basis set. The active space used for all bound-state calculations comprises the O(1s) orbital in RAS1, allowing for a single hole; RAS2 contains all 21 valence orbitals at full flexibility; RAS3 holds the lowest 5 virtual orbitals, allowing for a single electron. The wave functions, i.e., molecular orbital (MO) and configuration interaction (CI) coefficients for all investigated manifolds of electronic states were obtained in, respectively, independent state-averaged (SA) RASSCF calculations including all corresponding electronic configurations supported by the active space. For neutral aminophenol, 106 valence-excited states have been included in the SA-RASSCF optimization; 2226 valence-ionized and 211 O(1s)-ionized states have been included for the cation; 15631 (22260) valence-doubly-ionized and 2226 (3276) O(1s)-and-valence-ionized states for the respective singlet (triplet) dication species. To obtain the cation and singlet and triplet dication O(1s)-hole state manifolds, the 'HEXS' keyword of the OPENMOLCAS RASSCF implementation [71] has been used to remove configurations with a doubly occupied O(1s) orbital from the CI expansion during the SA-RASSCF optimization, which has in all cases been started from the MOs optimized for the manifold of valence-ionized cation states. To keep the hole-bearing O(1s) orbital in the RAS1 active space during the respective RASSCF procedures, avoiding collapse of the optimization to the energetically lower-lying valence manifold, the carbon and nitrogen 1s orbitals have been frozen and the 'supersymmetry' keyword has been used to prevent orbital rotations between all (carbon, nitrogen, and oxygen) 1s orbitals and the valence MOs. This leaves the O(1s) orbital unchanged during the optimization of the cation and dication O(1s)-hole state manifolds, so that it corresponds to the O(1s) orbital optimized for the valence-ionized aminophenol cation states. However, the valence MOs and CI coefficients are optimized independently in each case.

The cation valence manifold yields the tentatively assigned RAS3 orbital character $2 \times \pi^*$, $\sigma(\mathrm{Ryd}, 3s)$, and $2 \times \sigma(\mathrm{Ryd}, 3p)$. The obtained active spaces for the other manifolds of states are similar, however, the amount of admixed Rydberg character in RAS3 decreases with increasing

charge. The RASSCF energies of all manifolds of electronic states have been perturbatively corrected for dynamic correlation with the single-state RASPT2 method [72], using an IPEA shift of 0.25 a.u. and an imaginary shift of 0.5 a.u. Such computational setups have been shown to yield good agreement with a wide range of static and dynamic experimental X-Ray spectroscopic measurements [71, 73, 74, 75].

The Dyson orbitals for the pump-ionization have been evaluated with the Spherical Continuum for Auger-Meitner decay and Photoionization (SCAMPI) code [76, 77].

The O($1s$) absorption dipole moments have been evaluated between the valence and O($1s$)-hole state manifolds of the cation and dication with the RASSI method [78]. In that the customary rediagonalization of the Hamiltonian, constructed from the joint valence and O($1s$)-hole state manifolds, has not been carried out to avoid mixing both manifolds, which would considerably complicate the propagation of the dynamics. We expect this to be a reasonable assumption for the present study since the residual overlap matrix elements between the valence and O($1s$)-hole states are comparatively small.

SXD Continuum Calculations Details of the static-exchange B-spline DFT method implemented in Tiresia [57, 61] can be found elsewhere [60, 58]. A reference ground-state DFT electron density of p-aminophenol was obtained with the LB94 functional in the basis of *TZP* Slater-type orbitals with the ADF package [79], which was then used to evaluate the LB94 static-exchange DFT Hamiltonian in the B-spline basis. The basis has been build up from a one-center radial expansion of B-splines with a maximum order of 10, originating at the center of the aromatic ring and extending up to $R_{\mathrm{max}} = 22.5$ a.u. with a 0.15 a.u. stepsize and augmented by an additional knot at every radial atomic position. The angular functions for this long-range expansion are constituted by spherical harmonics of angular momenta up to $l_{\mathrm{max}} = 33$. The one-center basis was then augmented with small B-spline expansions at all atomic positions employing $l_{\mathrm{max}}^{\mathrm{H}} = 1$ (hydrogen) and $l_{\mathrm{max}}^{\mathrm{O,C,N}} = 2$ (other atoms) with a short range of 0.6 a.u. (carbon) and 0.7 a.u. (other atoms), respectively. Photoionization dipole moments have been evaluated between all $(l_{\mathrm{max}} + 1)^2 = 1156$ degenerate continuum orbitals obtained at 51 kinetic energies spanning 5.0-10.0 a.u. in 0.1. a.u. steps and the 2226 pump-ionization Dyson orbitals, one for every ionization transition from the neutral ground state to a valence-ionized cationic state, projected to the B-spline basis [62, 59].

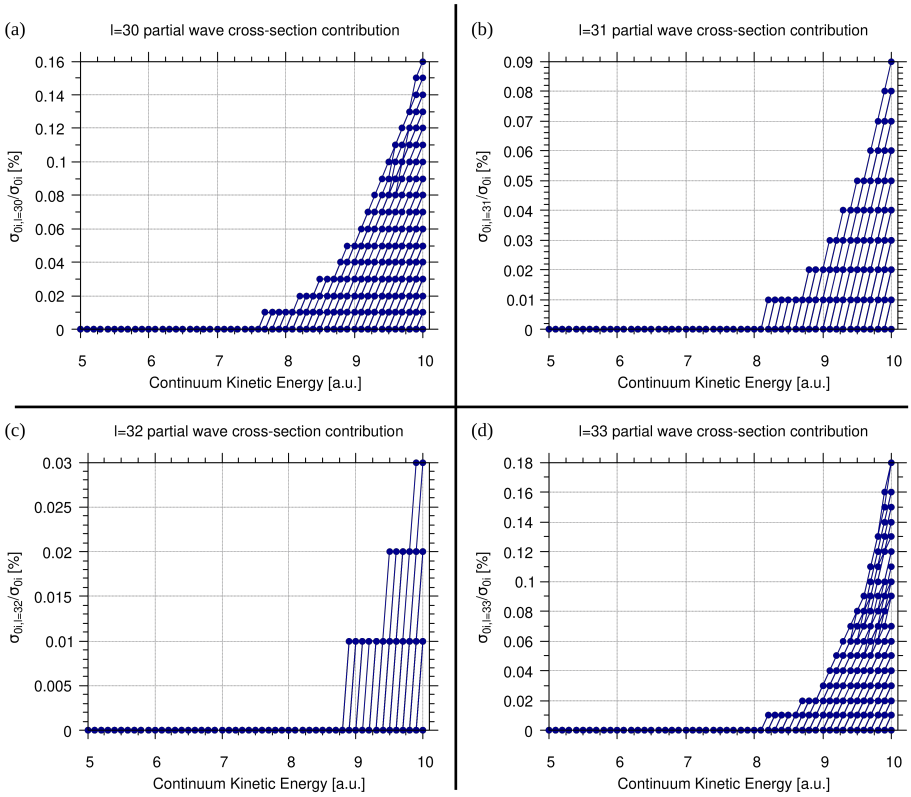

Figure S1: Relative contributions, in %, of the partial waves with the highest angular momenta included in the SXD B-spline basis, l = 30, 31, 32, and 33 to the ionization cross sections, $\sigma_{i,l}(\varepsilon)/\sigma_i(\varepsilon)$, for all $i = 1, ..., 2226$ cation states.

Regarding the convergence of the SXD B-spline basis. The relatively compact size of the radial grid is afforded within the SXD method implemented in Tiresia by allowing the last B-spline to be nonzero at $R_{\max}$. Employing a Galerkhin approach [80, 81], one then obtains $(l_{\max}+1)^2$ degenerate continuum orbitals at each kinetic energy that flexibly assume nonzero values at the boundary. The S-matrix normalization of the continuum orbitals is then obtained by matching these solutions to the appropriate asymptotic boundary conditions for photoionization at $R_{\max}$, which, consequently, only needs to extend just beyond the region of nonzero multi-centric molecular potential [57, 61].

To verify that the so-defined B-spline basis properly describes the short-range multi-centric molecular region, the MO energies obtained with a LB94 B-spline SXD calculation of the aminophenol ground state density have been compared with the MO energies obtained with the aforementioned respective initial ADF Slater Type orbital DFT calculation. Across all 29 occupied MOs, the B-spline SXD method yields MO energies that are on average 0.14 eV higher than the ADF MO energies, with a maximum deviation of 0.27 eV in the core shell. Considering only the 21

valence MOs, the average deviation is 0.11 eV, with a maximum of 0.15 eV, indicating satisfactory convergence for the molecular region. The radial basis, employing a maximum stepsize of 0.15 a.u., which is a factor of 9.4 times smaller than the wavelength obtained for the maximum continuum kinetic energy of 10.0 a.u., ensures enough flexibility to describe the rapid oscillations of the continuum wave functions [57]. The convergence of the angular momentum expansion to describe the continuum partial waves is demonstrated in Fig. S1. It shows a maximum relative contribution of $\frac{\sigma_{i,l}(\varepsilon)}{\sigma_i(\varepsilon)} \leq 0.2\%$ for the four highest included angular momenta, $l = 30, 31, 32, 33$, to the cross sections for all $i = 1, ..., 2226$ cationic states over the included kinetic energy range of $\varepsilon = 5.0 - 10.0$ a.u. The cross section for every cation state i is obtained as the sum over all angular momentum, l, and magnetic quantum number, m, partial-wave contributions, $\sigma_{i,l,m}(\varepsilon)$,

$$\sigma_i(\varepsilon) = \sum_{l=1}^{l_{\max}} \overbrace{\sum_{m=-l}^{l} \sigma_{i,l,m}(\varepsilon)}^{\sigma_{i,l}(\varepsilon)} \ . \tag{S16}$$

1.1.5 Extended RAS-SXD data

Analysis Of the Coherent Electron Dynamics at the Oxygen Site For the polarization averaged p-aminophenol cation density matrix right after the pump, $\gamma^+_{ij}(T_1)$, Fig. S2a depicts the degree of coherence, $g_{ij} = \frac{|\gamma^+_{ij}(T_1)|}{\sqrt{\gamma^+_{ii}(T_1)\gamma^+_{jj}(T_1)}}$, for the 125 stable cation states lying below the DIP. While the degree of coherence shows all coherences contained in the density matrix irrespective of their absolute weight, one needs to combine this data with the populations, indicated in the panels above and on the left of the matrix, to obtain the actual weight of the terms for the coherent dynamics. This combination is carried out in Fig. S2b, depicting the absolute off-diagonal density matrix elements. Here a logarithmic scale has been chosen, spanning values between 1.0E-4 and 1.0E-2, disregarding terms smaller than 1.0E-4 from the plot for the sake of clarity. The plot demonstrates that strong (orange-red) coherences are found between states lying between 10-15 eV of binding energy, as well as between 15-20 eV, albeit the latter seemingly appear preferentially at lower energetic separations, i.e. lower frequencies. Note that although the size of the colored tiles, each corresponding to a pair of cation states, reflects the density of states along the x and y binding energy axis, it is not related to the weight of the associated coherence, which is exclusively given

by the color code. To better visualize the population distribution in the region of the breakdown of the orbital picture above 15 eV, where the density of states rapidly increases, the red lines in the population panels depict the pump photoionization spectrum that is also depicted in Fig. 4a of the main text.

To find the most relevant contribution to the dynamics, a Fourier analysis has been conducted of the coherent hole charge fluctuation at the oxygen atom, which has been obtained, as for Fig. 2 of the main text, by integrating the hole density, Eq. (S11), over a 1.0 a.u. sphere around the oxygen atom. At variance with the results in the main text, however, here only the stable cationic states below the DIP of 20.745 eV are taken into account, corresponding to the portion of the density matrix depicted in Fig S2. The Fourier analysis of the oxygen hole charge reveals the individual oscillatory contributions for every coherence, i.e., tile in Fig S2, and their complex coefficient, allowing to sort them by their absolute weight, and to re-evaluate the coherent hole charge, taking into account only a limited number of contributions, which allows to study the convergence. This has been carried out in Fig. S3, where the oxygen hole charge dynamics is depicted for taking into account the most important 3, 5, 10, 100, 1000, and all 7750 coherent contributions of the polarization-averaged p-aminophenol cation density matrix. While convergence is reached with the 1000 most important contributions, one can see that central features of the dynamics are already obtained when accounting for just the 3 most important terms, in particular beyond delays of 3.5 fs. One should note that their summed weight is smaller than the cumulative weight of the remaining coherent terms, which, in turn, largely cancel each other, so that the rough main features of the dynamics are already obtained with the most important 3 contributions. At shorter times, the difference between the results employing the 3 most important and all coherences is somewhat larger, but already considerably improved when incorporating the 10 most important coherences. Including the 100 most important contributions is already close to convergence.

The respective 3 most important coherences are characterised in Table S1. They correspond to states lying between IPs of 10 eV and 15 eV with oscillation periods of 1.53 fs, 1.91 fs, and 2.78 fs, considerably shorter than the ADC prediction, see Fig. 4 of the main text. The respectively involved states, 3, 8, 9, 10, 16, are also indicated with green population sticks in Fig. S2. The assignment of these states is given in Fig. S4 in terms of the leading orbital excitations (electronic configurations) contributing to their CI expansion. In all cases the leading excitations are of HOMO-X $\rightarrow$ HOMO

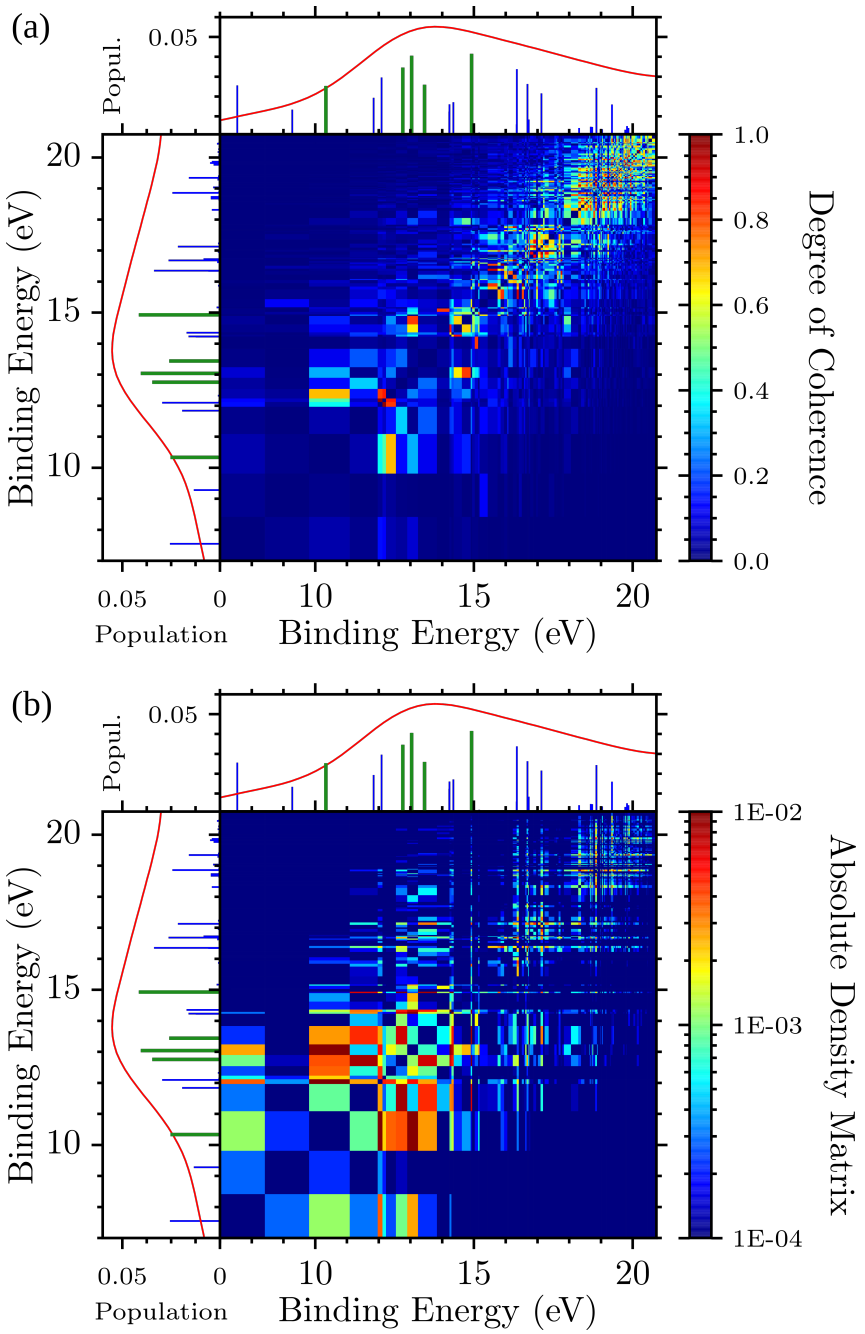

Figure S2: For the cation states below the DIP of 20.745 eV that do not autoionize, panel (a) depicts the off-diagonal degree of coherence obtained with the RAS-SXD approach, on a linear color scale and panel (b) the corresponding absolute off-diagonal density matrix elements, $|\gamma^{+}_{ii}(T_1)|$, on a logarithmic scale, to highlight the terms relevant for the coherent dynamics. The populations of each individual state, $\gamma^{+}_{ii}(T_1)$, (blue sticks), and photoionization spectrum (red) are given along the binding energy axes to visualize the population distribution. Green thick sticks correspond to the populations of the five states, 3, 8, 9, 10, 16, which constitute the three most important coherences for the charge dynamics at the oxygen site, see Table S1 and Fig. S3.

#	Cation States (i,j)	IP(i) , IP(j) [eV]	ΔE [eV]	Period T [fs]
1	(8,16)	12.76, 14.93	2.17	1.91
2	(3,9)	10.34, 13.04	2.70	1.53
3	(10,16)	13.44, 14.93	1.49	2.78

Table S1: For the three most important coherent contributions to the dynamics at the oxygen site of the p-aminophenol cation obtained with the RAS-SXD method, the table indicates the indices of the cation state pairs, the respective ionization potentials (IPs), the energy difference (oscillation frequency) and the oscillation periods.

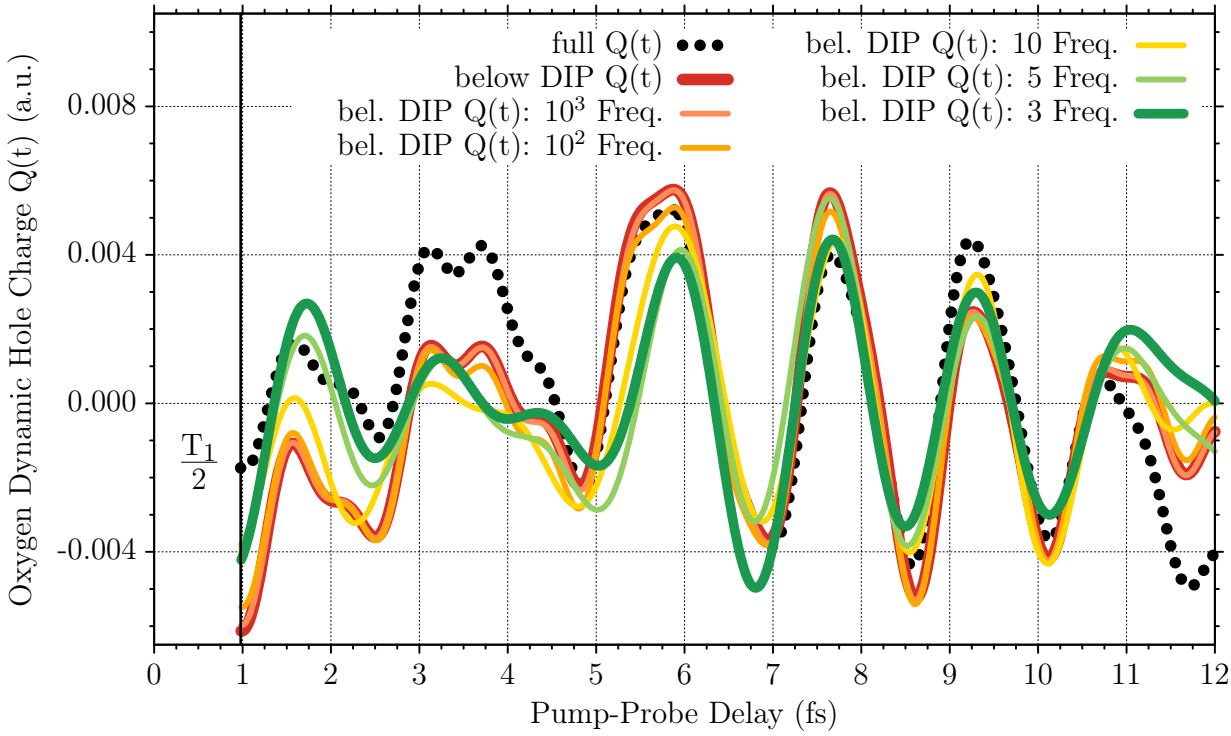

Figure S3: RAS-SXD simulation of the coherent fluctuations of the hole charge at the oxygen atom induced by the pump-ionization. The local hole charge has been obtained by integrating the dynamic hole density, Eq. (S11), over a 1.0 a.u. sphere around the oxygen atom, as in the main text. It is depicted for including in the evaluation of the dynamic trace the most important 3 (green, thick), 5 (light green), 10 (yellow), 100 (orange), 1000 (salmon), and all 7750 (red, thick) coherent terms of the cation density matrix below the DIP of 20.745 eV, corresponding to the stable cation states. A characterization of the three most important coherences is given in Table S1 and Fig. S4. The respective portion of the density matrix is depicted in Fig. S2. For orientation, the oxygen hole-charge dynamics obtained from the full density matrix and disregarding autoionization, the same as depicted in Fig. 2 of the main text, is given by the black dotted curve.

character, with X$\leq$ 10, involving $\pi \rightarrow \pi$ (state 3) as well as $\sigma \rightarrow \pi$ (state 16), and mixed $\sigma/\pi \rightarrow \pi$ (states 9 and 10) character. Excitations from lower lying bound as well as to the virtual (Rydberg) orbitals are of lesser importance for these states. However, these terms are contributing to the weight

not covered by the main configurations depicted in Fig. S4. This multi-configurational nature is in part a consequence of the strongly mixed RASSCF orbitals that are obtained from the state-average over 2226 valence states of the cation, see Sect. 1.1.4, however, for higher lying states, it reflects the multi-configurational character due to the breakdown of the orbital picture, see Fig. S2.

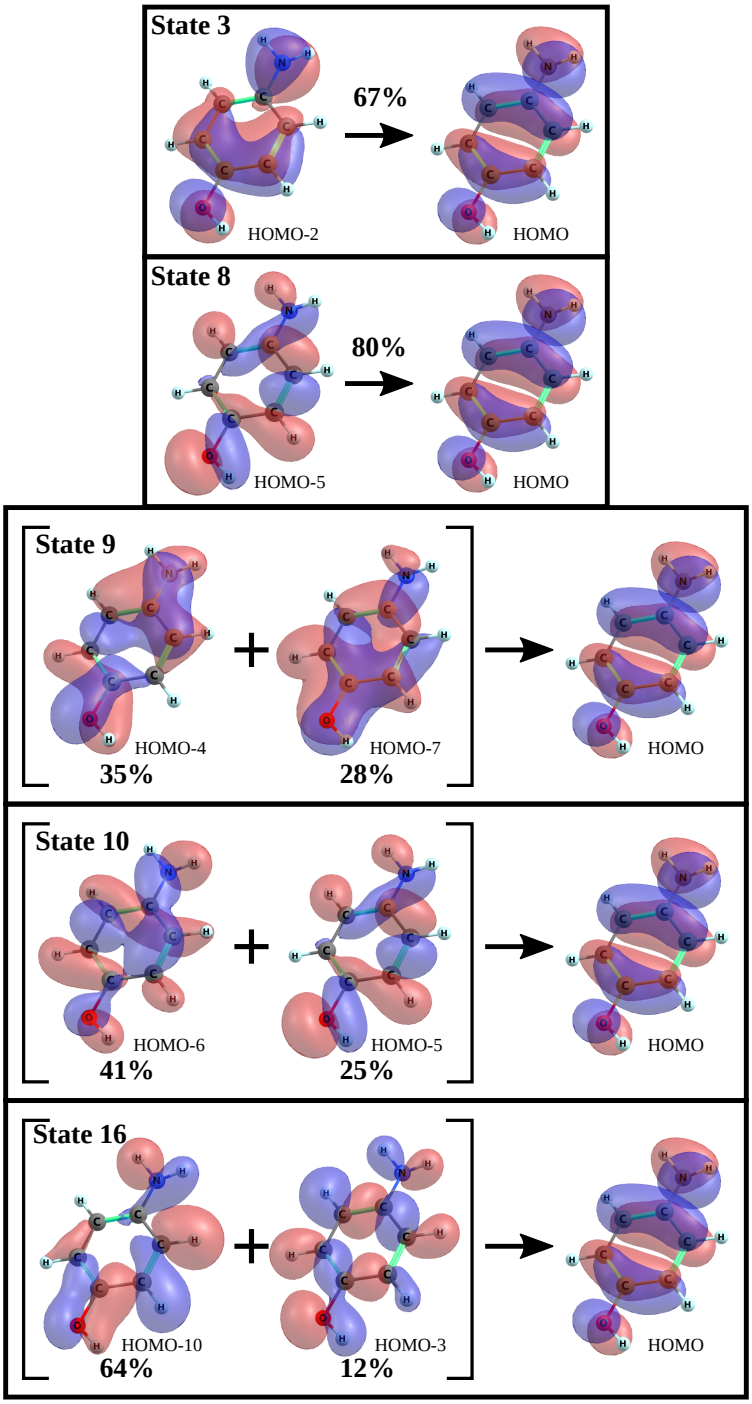

Figure S4: Characterizations of the excited states of the p-aminophenol cation involved in the three most important contributions to the coherent dynamics predicted with the RAS-SXD method at the oxygen site, see Table S1. For each state the primary excitation contributions, i.e., with a weight larger than 10%, are depicted in terms of the involved molecular orbitals obtained by the state-averaged RASSCF procedure taking into account all 2226 cation states, see sect. 1.1.4 for details. The weights of the respective excited electronic configurations, indicated as percentages, have been inferred from the CI-expansion of each state.

Analysis of the Cation and Dication trXAS Fig. S5 compares the total (purple) and dication (blue) RAS-SXD trXAS at a delay of 0.54 fs, incorporating a shift of 4 eV into the dication absorption feature (solid) with those employing the unshifted dication trXAS (dashed) and against the experimental trXAS for a delay of 0.49 fs depicted in Fig. 4b of the main text. The cation trXAS spectrum (red) remains unshifted and is also given for orientation. Shifting the dication trXAS by 4 eV improves the agreement of the total (cation + dication) trXAS with the experimental reference data at a delay of about 0.5 fs.

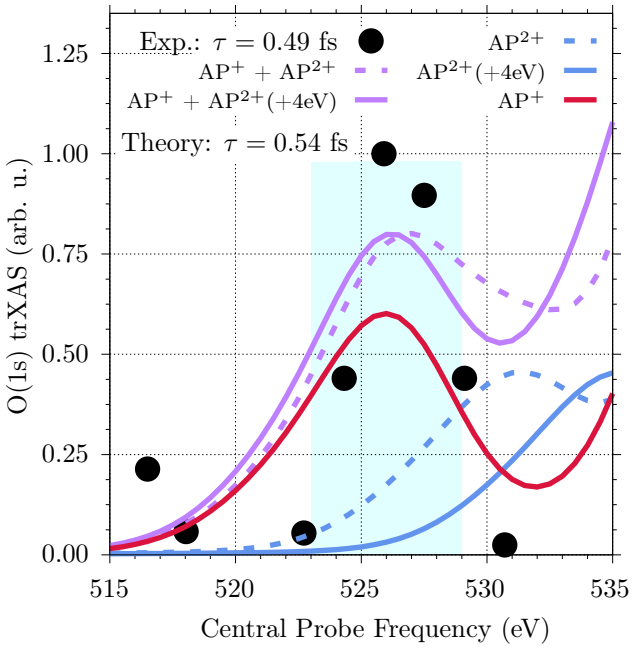

Figure S5: Experimental trXAS at a delay of $\tau = 0.49$ fs (black dots), from Fig. 4 of the main text, and total RAS-SXD $\tau = 0.54$ fs trXAS (p-AP^{+}+p-AP^{2+}, purple), decomposed into the cation (p-AP^{+}, red) and dication (p-AP^{2+}, blue) contributions. To augment the agreement of the total RAS-SXD signal with the experimental data, the simulated dication trXAS has been shifted by 4 eV to obtain the solid blue and purple lines. The results without this shift are given for orientation as dashed lines; the cation trXAS remains unshifted in both cases. The total trXAS curves have been respectively normalized to yield the same maximum value and the normalization for the unshifted total trXAS (dashed, purple) has been used to scale the cation and dication curves. The experimental data has been normalized to 1.0 at its maximum.

Fig. S6a and b depict the RAS-SXD total trXAS (purple) decomposed into the contributions from the cation (red) and dication (blue), with (A.I.) and without including autoionization (no A.I.) due to Super Coster-Kronig Decay. The cation trXAS evaluated without autoionization (brown) is further decomposed into the contributions of states above (green) and below the DIP (yellow).

Panel a depicts the time traces obtained by integrating the trXAS over the interval of 523-529 eV of photon energy, as indicated in panel b for the delays of 0.54 fs (solid) and 1.70 fs (dashed). In that, the dication trXAS has been shifted by 4.0 eV as discussed for Fig. S5. With autoionization, the trXAS of the cation states above the DIP decays while the dication trXAS increases. This essentially reflects the population dynamics illustrated in panel c. The contribution of the states below the DIP, however, is not affected by the autoionization, and in fact carries most of the coherent dynamics.

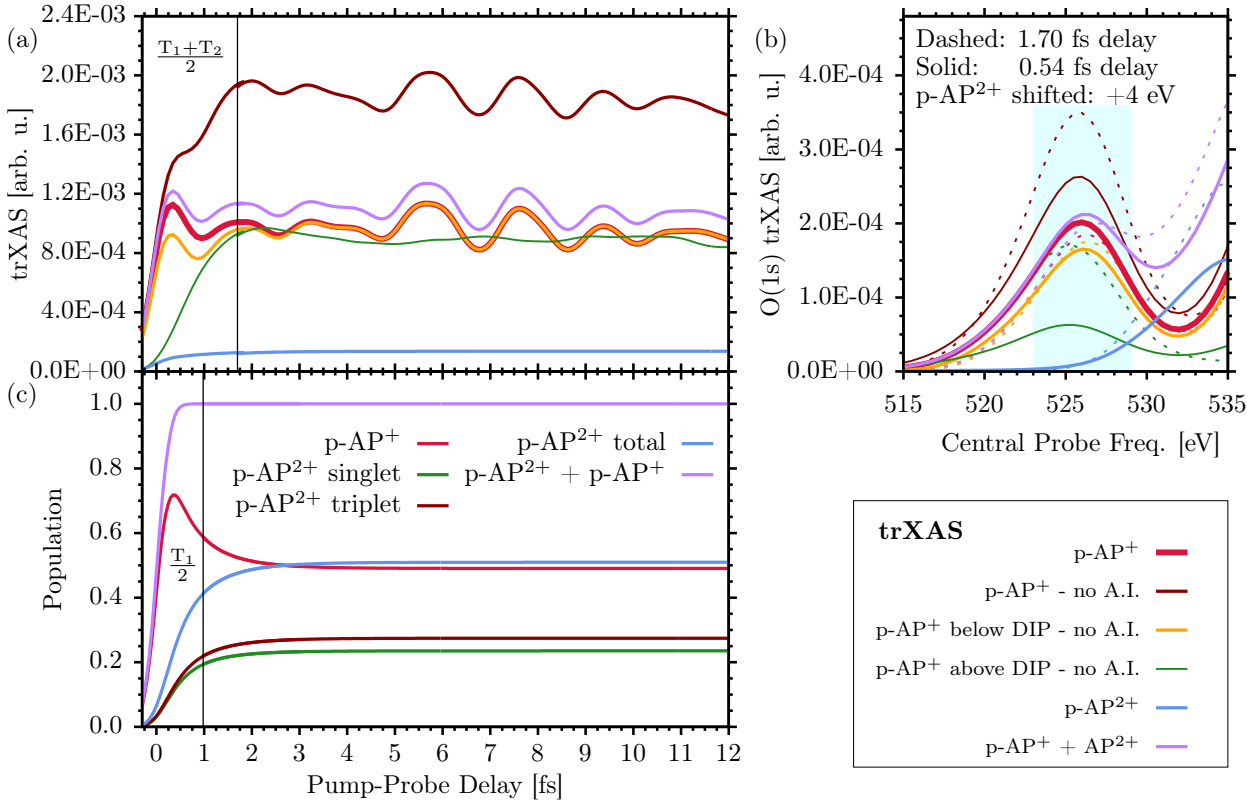

Figure S6: (a) trXAS traces obtained with the RAS-SXD method for the p-aminophenol cation (p-AP$^+$, red), dication (p-AP^{2+}, blue), and their sum, (p-AP$^+$+p-AP^{2+}, purple), i.e., the total signal discussed in Fig. 4 of the main text. The cation trXAS without autoionization (no A.I., brown) and its decomposition into contributions from states below (yellow) and above (green) the DIP are also indicated. (b) Corresponding photon-energy resolved trXAS at a delay of $\tau = 0.54$ fs (solid lines) compared to those at $\tau = \frac{T_1+T_2}{2} = 1.7$ fs, where the pulses do not overlap anymore (dashed lines) using the same color code as in panel (a). The dication trXAS has been shifted by +4 eV to higher photon energy before integrating over the photon energy window of 523-529 eV indicated by a light-blue rectangle. (c) Population dynamics of the p-aminophenol cation and dication species.

1.2 ADC Model

Theoretical modeling and simulation of the photoionization dynamics triggered by the x-ray laser pulses in the para-aminophenol molecule are performed for the method labeled 'ADC' within the framework of the time-dependent B-spline restricted correlation space (RCS) – algebraic diagrammatic construction (ADC) *ab initio* methods [55, 9, 82, 83]. Both interactions of the neutral para-aminophenol molecule with the pump and of its cation with the probe x-ray attosecond pulses, respectively, are described from-first-principles at the equilibrium geometry of neutral para-aminophenol.

1.2.1 Simulation of x-ray attosecond pump ionization

Within the B-spline RCS-ADC method, a multicenter B-spline basis set [58, 55] is used to describe single-electron states. The space of the unoccupied states resulting from a Hartree-Fock (HF) calculation is partitioned into two orthonormal subspaces: the restricted correlation space (RCS) (χ_α), designed to accurately describe the localized short-range correlation of the system, and its orthonormal complement, the ionization space (IS) (ψ_μ), which describes the long-range part of the photoelectron wavefunction and complements the RCS space in order to represent the electronic wavefunction throughout the entire spatial region [55]. Here and in what follows, the $\alpha, \beta, ...$ and $\mu, \nu, ...$ indices refer to the virtual space (unoccupied) RCS and IS orbitals, respectively, whereas $i, j, k, ...$, indicate the occupied HF molecular orbitals. In the simulation, we used a B-spline basis characterized by a radius of the radial box $R_{max} = 80$ a.u., a linear radial grid with step size $h = 0.45$ a.u., and a maximum value of orbital angular momentum $L_{max} = 12$. The RCS orbital space consists of the virtual orbitals from an HF calculation performed in the cc-pVDZ GTO basis set.

Within the time-dependent (TD) B-spline RCS-ADC(n) approach to molecular photoionization dynamics [55, 9, 82, 83], the 3D time-dependent Schrödinger equation (TDSE) for the N-electron polyatomic para-aminophenol molecule interacting with the pump laser pulse

$$i\hbar \frac{\partial |\Psi^N(t)\rangle}{\partial t} = \hat{H}^N_{Pump}(t) \, |\Psi^N(t)\rangle \tag{S17}$$

is solved non-perturbatively, by expanding the TD many-electron wavefunction on the basis of the

ground and excited RCS-ADC(n) states [9, 82, 13]

$$|\Psi^N(t)\rangle = \sum_{m,\mu} c_{m,\mu}(t)\, \hat{a}_\mu^\dagger |\Phi_m^{N-1,RCS}\rangle + \sum_{I_{RCS}} c_{I_{RCS}}(t)\, |\tilde{\Psi}^N_{I_{RCS}}\rangle^{[n]} + c_0(t)\, |\Psi_0^{RCS}\rangle^{[n]}. \tag{S18}$$

Here $|\Psi_0^{RCS}\rangle^{[n]}$ is the n-th order RCS correlated ground state, and $|\tilde{\Psi}^N_{I_{RCS}}\rangle^{[n]}$ indicate the excited intermediate states of the nth-order ADC(n) scheme for excitation of many-electron systems, built using the single-particle RCS basis. Within the first-order ADC(1) scheme ([n]=[1] in Eq. S18), the excited (N)-electron intermediate states span the configuration space consisting of one-hole – one-particle (1h1p) ($|\tilde{\Psi}^N_{\alpha i}\rangle^{[n]}$) excitation classes built on top of the HF ground state [84, 85], while the extended second-order ADC(2)x scheme, which is the one used in this work, also includes the configuration space consisting of two-hole – two-particle (2h2p) ($|\tilde{\Psi}^N_{\alpha\beta ij}\rangle^{[n]}$) excitation classes built on top of the RCS correlated ground state [55].

The first term on the right-hand side of Eq. S18 describes the IS configuration states of B-spline RCS-ADC, which take the form of ionization channel-specific product states and reads $|\Psi^N_{\mu,m}\rangle = \hat{a}_\mu^\dagger |\Phi_m^{N-1,RCS}\rangle$, where $\hat{a}_\mu^\dagger$ is the creation operator of an electron in the IS molecular orbital ψ_μ and $|\Phi_m^{N-1,RCS}\rangle$ denotes the RCS-ADC ionic eigenstates. In the ADC(1) scheme, the ionic eigenstates consist of 1h states where one electron is removed from any of the 21 occupied HF molecular orbitals of neutral para-aminophenol. In the RCS-ADC(2)x scheme, the $|\Phi_m^{N-1,RCS}\rangle$ states are obtained by diagonalizing the ionic Hamiltonian calculated at the ADC(2)x level of theory and using the single-particle RCS basis set

$$\hat{H}^{(N-1,RCS)}_{ADC(2)x} |\Phi_m^{N-1,RCS}\rangle = I_m^p |\Phi_m^{N-1,RCS}\rangle\,, \tag{S19}$$

where the ionization energy is given by $I_m^p = E_m^{(N-1)} - E_0^{RCS}$, E_0^{RCS} is the RCS energy of the correlated ground state of the neutral molecule, and the ionic states are expanded into one-hole (1h), and two-holes - one-particle (2h1p) configurations derived from the RCS ground state

$$|\Phi_m^{N-1,RCS}\rangle = \sum_i |\tilde{\Phi}_i^{N-1}\rangle + \sum_{\alpha ij} |\tilde{\Phi}_{\alpha ij}^{N-1}\rangle\,. \tag{S20}$$

The ansatz of Eq. S18 includes an explicit description of both electronic continua and many-body

electron correlation effects, such as shakeup processes and breakdown of the molecular orbital (MO) picture. Moreover, the TD B-spline RCS-ADC theoretical framework fully accounts for the interchannel couplings between different ionization channels in the continuum, which can play an essential role during the ionization event.

The total time-dependent Hamiltonian of Eq. S17 reads

$$\hat{H}^N_{Pump}(t) = \hat{\tilde{H}}^N_{RCS-ADC} + \hat{D}^N_{RCS-ADC} E_{Pump}(t) - i\hat{W}_{CAP}\,, \tag{S21}$$

where a quadratic complex absorbing potential (CAP) $\hat{W}_{CAP}(r) = \eta\,(r - R_{CAP})^2$ is used to eliminate wave packet reflections from the boundaries of the B-spline radial grid. The laser-molecule interaction is described within the dipole approximation in length form, and $\hat{\tilde{H}}^N_{RCS-ADC}$ and $\hat{D}^N_{RCS-ADC}$ are the representation of the shifted field-free Hamiltonian $\hat{\tilde{H}} = \hat{H} - E_0^{RCS}$ and the dipole operator $\hat{D}$, respectively, in the space of RCS-ADC intermediate states (see Eq. (2)). The values of the CAP parameters used are $\eta = 5 \times 10^{-3}$ and $R_{CAP} = 55$ a.u.

The time propagation of the unknown coefficients of the many-electron wavefunction in Eq. S18 is performed by means of the Arnoldi/Lanczos algorithm [86, 87, 9]. During the simulation of the pump step, we have included in the expansion of the many-electron wavefunction only the ionization channels with an (ionization) spectral intensity value (see refs. [55, 9, 13]) greater than 1 %. These states will be denoted in the following as $|\Phi^{N-1,RCS}_{m,Pump-ionized}\rangle$. The *ab initio* simulation of the pump step has been performed using a linearly polarized pulse, characterized by a Gaussian temporal envelope, a central frequency $\hbar\omega_{Pump} = 263$ eV, peak intensity $I_{Pump} = 5 \times 10^{12}$ W/cm^2 and bandwidth $\simeq 3$ eV (FWHM). Converged results have been obtained by using a 0.5 attosecond time-step and a 40-dimensional Krylov-space in the Arnoldi/Lanczos time propagation.

The electron dynamics, both during and after the interaction of para-aminophenol with the pump pulse, is obtained from the time-dependent reduced ionic density matrix (R-IDM) $\hat{\rho}^{R-IDM}(t)$ of the molecular ion, which is calculated by tracing out the unobserved photoelectron degree of freedom from the total time-dependent density matrix of the charge-neutral N-electron system

$$\hat{\rho}^{R-IDM}(t) = Tr_\mu \left[\langle \Psi^N(t) | \Psi^N(t) \rangle \right] . \tag{S22}$$

Within the TD B-spline RCS-ADC(n) framework, and using Eq. S18, the resulting R-IDM on the

basis of RCS-ADC(2)x ionic eigenstates reads

$$\rho_{m,n}^{R-IDM}(t) = \sum_{\mu} c_{m,\mu}(t) \left[c_{m,\mu}(t)\right]^{*} + 2e^{i\left(I_n^p - I_m^p\right)t} \times \int_{\infty}^{t} \sum_{\mu,\nu} w_{\nu,\mu} c_{m,\mu}\left(t'\right) \left[c_{n,\nu}\left(t'\right)\right]^{*} e^{-i\left(I_n^p - I_m^p\right)t'} dt', \tag{S23}$$

where the latter term corrects for the loss of norm introduced by the CAP [9], I_m^p is the ionization potential of the ionic state m and $\omega_{\nu,\mu}$ is the CAP matrix element between photoelectron IS orbitals ψ_ν and ψ_μ. From hereon in we shall omit the R-IDM superscript and denote the reduced ionic density matrix as $\rho_{m,n}$. The time-dependent population of the ionic eigenstates is given by the diagonal elements

$$P_m(t) = |\rho_{m,m}(t)|, \tag{S24}$$

while the off-diagonal ones $\rho_{m,n}$ are related to the degrees of quantum electronic coherence [47], $0 \leq G_{m,n} \leq 1$, between any pair of populated ionic channels m and n

$$G_{m,n}(t) = \frac{|\rho_{m,n}(t)|}{\sqrt{P_m(t) \times P_n(t)}}. \tag{S25}$$

Extended Data Fig. E4 shows the calculated 2D map of quantum electronic coherences $G_{m,n}$ between the ionic states of para-aminophenol, as it results from the TD B-spline RCS-ADC(1) (Fig. E4 A) and RCS-ADC(2)x (Extended Data Fig. E4 B) simulations respectively. The final stationary populations $P_m(\infty)$ of the ADC(1) and the bound ADC(2)x-calculated eigenstates of the para-aminophenol cation are also shown in the vertical and horizontal side panels of Extended Data Fig. E4. In the calculations presented here, all the ionic time-dependent populations $P_m(t)$ have converged to their final stationary value at $t \approx 100$ attoseconds after pump ionization. The ADC photoelectron spectrum shown in Fig. 4a is obtained by using the t-surf technique [88], and using a t-surf radius $R_{t-surf} = 40$ a.u.

1.2.2 Simulation of x-ray attosecond probe absorption

We explicitly simulated the interaction of the pump-ionized system with the probe pulse and calculated the time-delay dependence of probe-induced x-ray absorption from the pump-ionized para-aminophenol cation in order to obtain a realistic description of the observable measured in the

experiment.

The formal validity of the presented theoretical results relies on non-overlapping pump and probe pulses. In practice, this limits the pump-probe time-delays that can be accurately described to the ones greater than half the duration of the x-ray pump pulse, i.e. in this case to delay times larger than ≈ 0.7 femtoseconds. In the ADC calculation, delays for which the pump and probe pulse are overlapped can be approximated by artificially truncating the pump pulse, meaning the pump and probe pulse are never simultaneously present in the calculation. The non-perturbative, time-dependent description of the cation-probe interaction is performed by solving the time-dependent von Neumann equations [82, 13] for the characterized reduced ionic density matrix (Eq. (7)) interacting with the probe laser

$$\frac{d\hat{\rho}\,(t)}{dt} = \frac{i}{\hbar}[\hat{H}^{N-1}_{Probe}\,(t)\,,\hat{\rho}\,(t)]. \tag{S26}$$

The probe-cation interaction is also described within the dipole approximation in length form. Eq. S26 is solved in this work by representing the ionic density matrix both in the valence-ionized states populated by the pump process $|\Phi^{N-1,RCS}_{m,Pump-ionized}\rangle$, and the core-ionized states $|\Phi^{N-1,RCS}_{m',Core}\rangle$, which are accessible to the probe pulse but were not populated in the pump ionization step. The probe pulse used in the simulation is characterized by a central photon energy $\hbar\omega_{Probe} = 526$ eV, peak intensity $I_{Pump} = 10^{12}$ W/cm^2 and bandwidth $\simeq 5$ eV (FWHM). The 526 eV photon energy can induce transitions from the valence-ionized states to core-ionized resonances $|\Phi^{N-1,RCS}_{m',Core}\rangle$ of the para-aminophenol cation in the energy range of the oxygen K-edge, which are described here at the RCS-ADC(3) level of theory and employing the core-valence approximation. Finally, the measurable XAS signal resulting from the interaction of the x-ray probe pulse with the pump-prepared cationic system is obtained by the final population of the O(1s) core-ionized resonances $|\Phi^{N-1,RCS}_{m',Core}\rangle$ upon interaction with the attosecond probe pulse.

In order to model the ultrafast super-Coster-Kronig (CK) decay of the cationic states with an energy above the double ionization potential (DIP) energy threshold, in the probe simulations we introduced a phenomenological, exponentially-decaying term to the ionic Hamiltonian, namely $e^{-\frac{t}{\tau_{CK}}}$. The decay lifetimes used in the simulation, which have been calculated *ab initio* by means of the Fano-ADC(2)x method [46], are: $\tau_{CK} = 345$ attoseconds for ionic states with energy above

the DIP, but below 23 eV; τ_{CK} = 425 attoseconds for states with energy between 23 eV and 30 eV; τ_{CK} = 864 attoseconds for states with energy between 30 eV and 34 eV. As a result, in the TD RCS-ADC simulation the population of the ionic states with energy above E_{DIP} is driven by the aforementioned dumping factor and, at the same time, by the pump laser that tends to increase it for short time-delays below 1.6 femtoseconds. However, it is important to note that also for time-delays where there is considerable overlap between the pump and probe pulses, the present theoretical modeling only considers independent pump and probe effects, which could influence the accuracy of the theoretical points for such short time-delays.

Extended Data Fig. E6 shows the RCS-ADC calculated XAS signal in the photon energy region from 518 to 535 eV. Both contributions of the RCS-ADC(2)x cationic states populated by the pump pulse below and above the DIP is shown.

Extended Data Fig. E5 shows the trXAS signal calculated with the RCS-ADC method, integrated in the photon energy region from 521 to 530 eV. Both contributions of the RCS-ADC(2)x cationic states populated by the pump pulse below and above the DIP is also shown.

The contribution to the XAS signal from the decayed cationic states is converted into absorption from the resulting dicationic populations (which will partially contribute to the same photon energy absorption window). The total trXAS signal can therefore be therefore decomposed into two contributions:

$$XAS^{TOT}(t) = XAS^{Cation}(t) + XAS^{Dication}(t) \ , \tag{S27}$$

where $XAS^{Cation}(t)$ describes the contribution from the cationic states below DIP and above DIP,

$$XAS^{Cation}(t) = XAS^{Cation}_{BelowDIP}(t) + XAS^{Cation}_{AboveDIP}(t) \ , \tag{S28}$$

and

$$XAS^{Dication}(t) = \alpha \times XAS^{DecayedCation}(t) \tag{S29}$$

describes the dication contribution to the XAS signal at time t as a percentage of the absorption contribution of the cationic states that have already undergone super-CK decay at time t. In other words, the contribution of the unbound ionic states is added back, as it decays (see the green curve in Extended Data Fig. E6), multiplied by a factor α to the total XAS signal. The case α = 1

corresponds to a scenario in which the overall dicationic population absorbs into the probe photon energy window (523-531 eV in the ADC calculation) exactly as much as the cationic states that have decayed (super-Coster-Kronig) would have done.

In Fig. 4, an additional exponential decay factor is added to the calculated XAS signal in order to model a shift of the absorption window driven by nuclear motion, which should indeed lead to a decay of the background XAS signal.

2 Contribution from Higher Harmonics of the XFEL

Free-electron laser radiation can include a small contribution from higher order harmonics of the fundamental, most notably an on-axis contribution from the third harmonic at the sub-to-few percent level [89]. Our measurements of the x-ray spectrum and photoelectron spectrum confirmed that the first set of undulators also generated a small amount of on-axis radiation at the third harmonic of the pump photon energy (3ω~780 eV). We studied the behavior of the third harmonic pulse energy and found it to be approximately linear with the pump (260 eV) pulse energy, as shown in Extended Data Fig. E3A. Moreover, the pulse energy of the third harmonic also showed a weak correlation with energy of the electron beam, as shown in Extended Data Fig. E3D.

To quantify the contribution of the third harmonic to the measured Auger-Meitner electron signal, we recorded data with the the K-value of the probe undulators randomized, to suppress the lasing of the probe pulse. We then measured the number of electrons produced by third harmonic in the same electron kinetic energy range analyzed in the experiment (420 – 550 eV), and using the same magnetic bottle electron spectrometer configuration. The proportionality constant $\alpha(\gamma_{beam})$, between the pump pulse energy and the number of electrons produced by the third harmonic, was calculated for different electron beam energies (γ_{beam}). For each shot in our pump/probe scan, we then performed a background subtraction using this measured proportionality constant, according to

$$\tilde{\vec{b}} = \vec{b} - \alpha(\gamma_{beam}) E_{pump} \tag{S30}$$

where $\vec{b}$ is the number of Auger-Meitner electrons recorded in a given shot, $\tilde{\vec{b}}$ is the value with the 3ω background removed, and E_{pump} is the pump pulse energy. This correction was applied prior

to the ghost imaging analysis.

Extended Data Figures and Tables

Delay Point	Simulated Pump-Probe Time-Delay	Shots per pump-pulse energy bin
1	489±67	5.2×10^4
2	706±94	2.2×10^4
3	957±127	1.4×10^4
4	1120±144	1.4×10^4
5	1835±138	1.1×10^4
6	5444±33	1.9×10^4
7	8112±33	2.2×10^4
8	11280±33	7.8×10^3

Table E1: The mean value and the systematic error of each time-delay point.

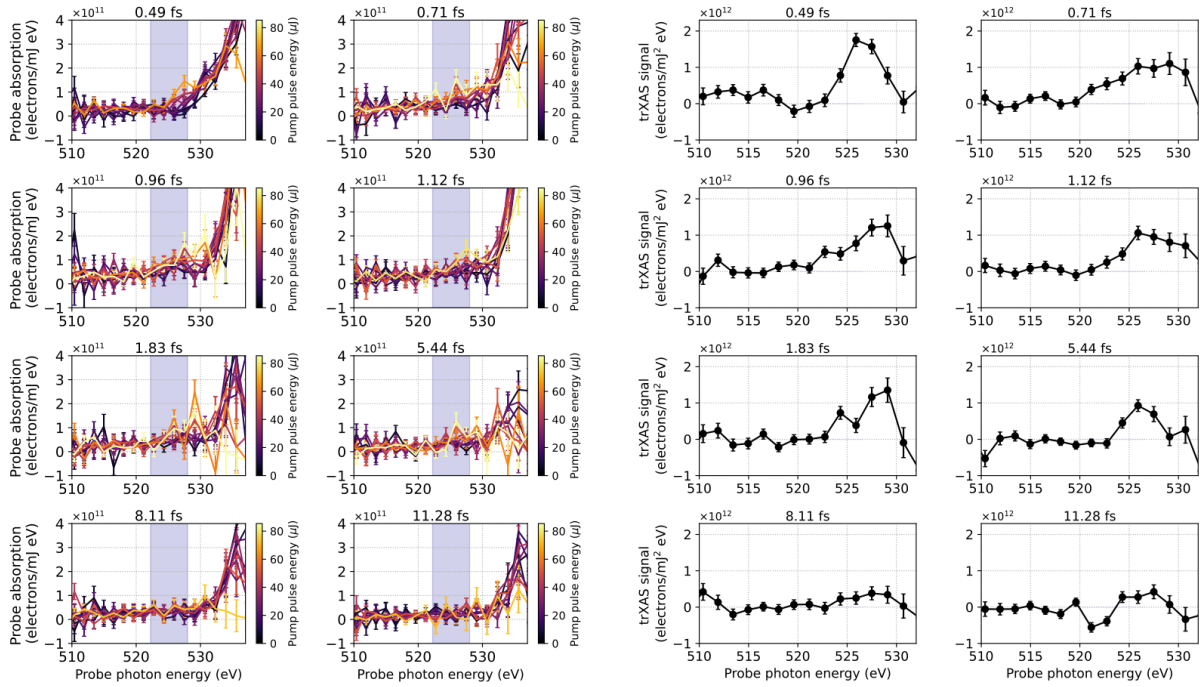

Figure E1: Left side: Sample absorption reconstructed for each pump pulse energy bin, indicated by the colorbar on the side of each figure. The shaded blue region is the area of integration where the trXAS signal is observed. Right side: Photon-energy-dependent trXAS signal regressed from the panels of the left side of the figure. The spectrum is resolved in photon energy, and has been smoothed by calculating a rolling average across two photon energy bins.

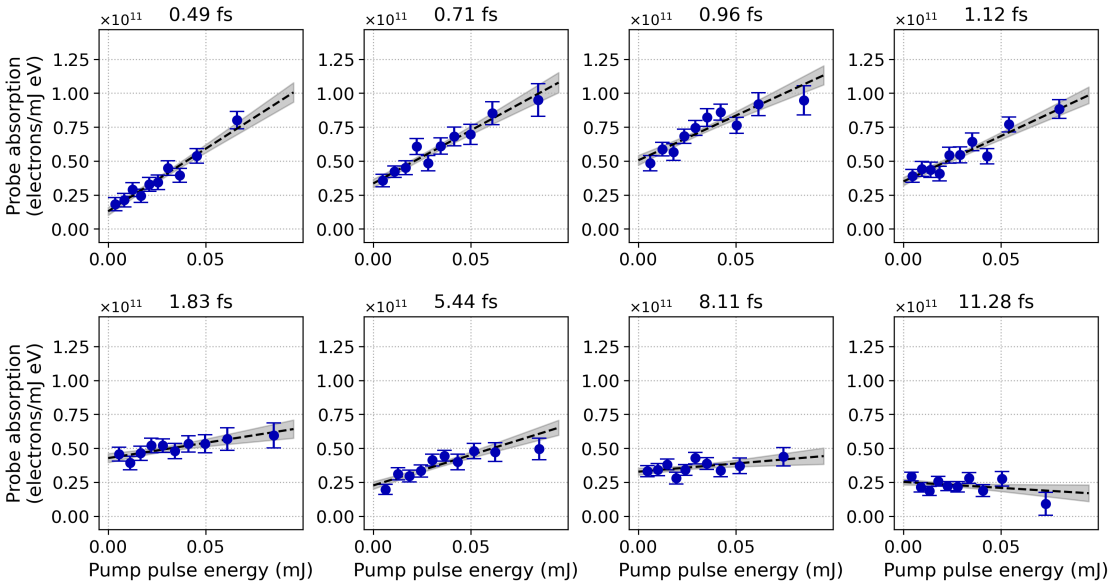

Figure E2: The integrated absorption yield is regressed on the pump pulse energy for each delay point and the pump/probe signal is extracted from the slope of the fit (dotted line). The gray region is the one standard deviation confidence interval for the fit, given the error bars in the integrated absorption yield.

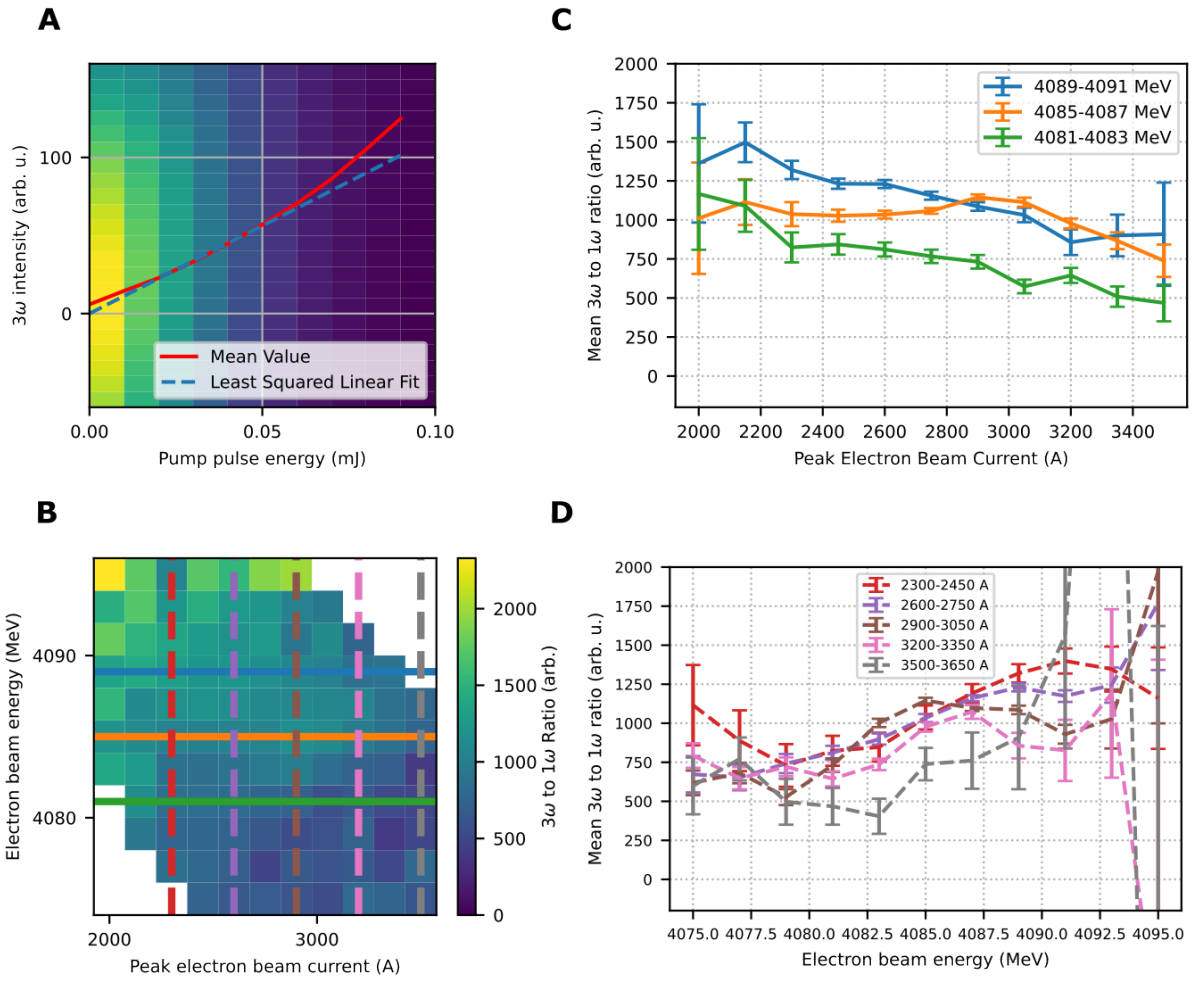

Figure E3: **a)** Pulse energy of the third harmonic contribution measured using the variable line spacing spectrometer (y-axis), as a function of pump pulse energy (x-axis). Color map represents the number of shots measured at each value of third harmonic pulse energy and pump pulse energy. **b)** Ratio of pulse energies in third harmonic and pump pulse (first harmonic), as a function of electron beam energy and peak electron beam current. **c)** Lineouts along the peak electron beam current axis while holding the electron beam energy fixed (indicated by colored lines in panel **b**). **d)** Lineouts along the the electron beam energy axis while holding the peak electron beam current fixed (indicated by colored lines in panel **b**).

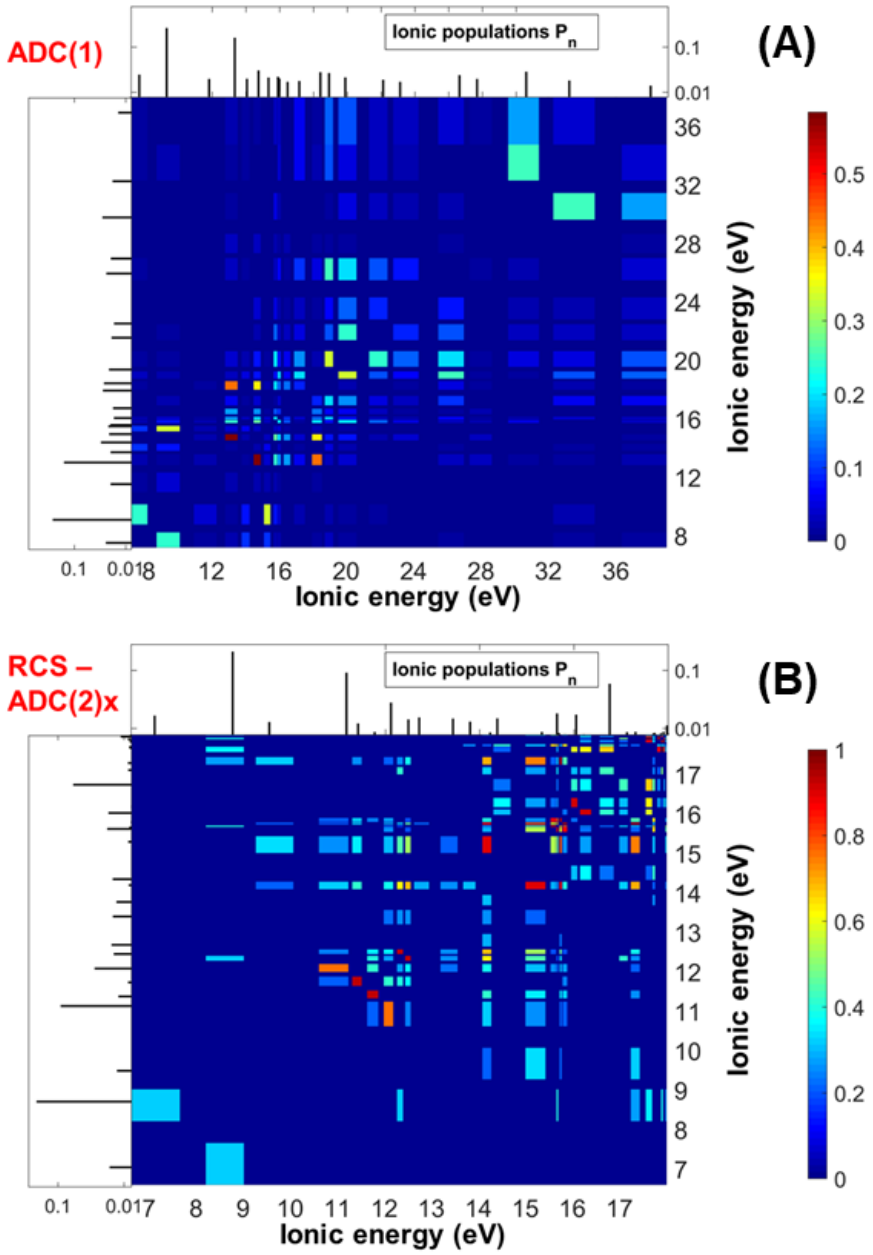

Figure E4: *Ab initio* TD B-spline RCS-ADC simulation of the pump-induced first ionization of para-aminophenol. The upper panel (A) shows the degrees of quantum electronic coherence $G_{m,n}$ (Eq. (9)) produced between each pair of ADC(1) cationic eigenstates populated by the pump pulse. The populations of the ionic eigenstates are also shown in the vertical and horizontal side panels. The lower panel (B) shows the degrees of quantum electronic coherence $G_{m,n}$ (Eq. S25) produced between each pair of bound RCS-ADC(2)x cationic eigenstates populated by the pump pulse. The populations of the ionic eigenstates, with energies $I_m^p < E_{DIP}$, are also shown in the vertical and horizontal side panels.

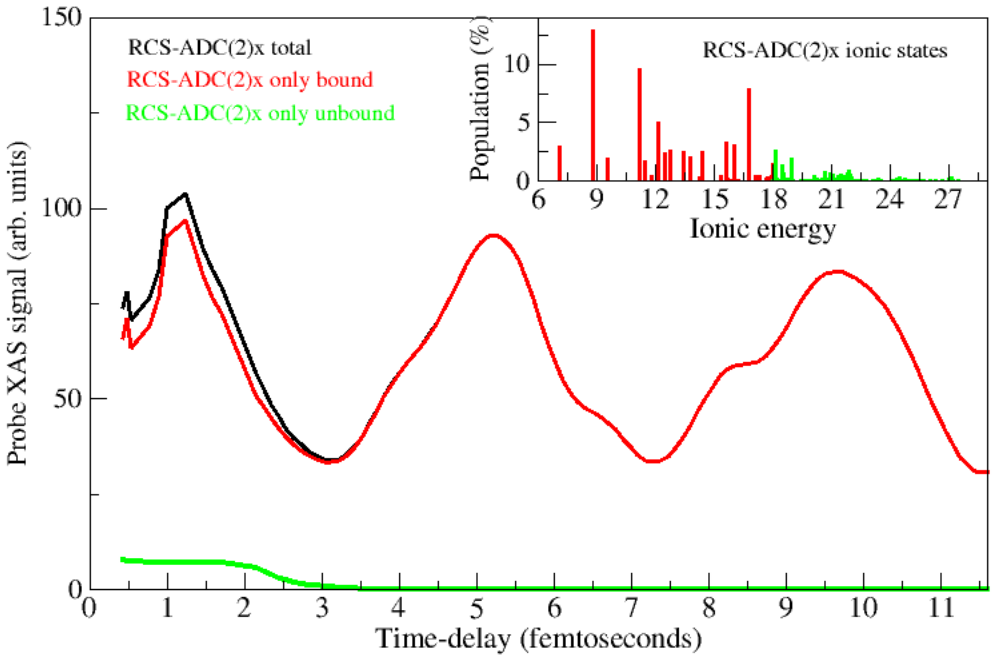

Figure E5: The trXAS signal calculated with the RCS-ADC method, integrated in the photon energy region from 521 to 530 eV. The red and green curve indicate the contribution of the bound (red sticks in the inset) and unbound (green sticks in the inset) RCS-ADC(2)x cationic states populated by the pump pulse, respectively. The total contribution of both bound and unbound states is shown by the black curve.

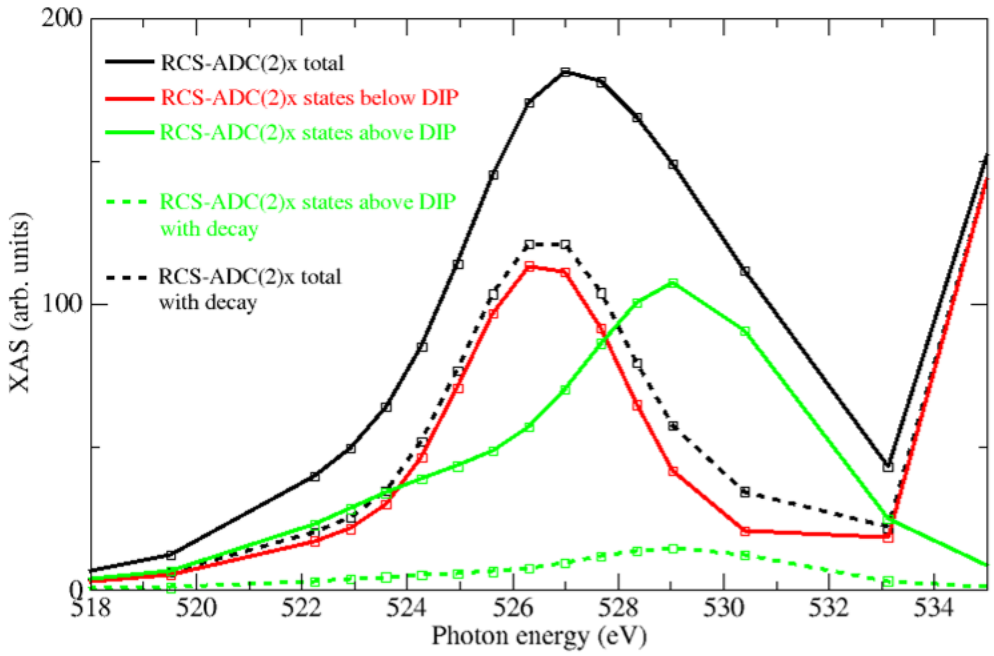

Figure E6: The RCS-ADC calculated XAS signal in the photon energy region from 518 to 535 eV. The red and green curve indicate the contribution of the RCS-ADC(2)x cationic states populated by the pump pulse below and above the DIP, respectively. The total contribution of both set of states is shown by the black curve. Full lines do not include the autoionization decaying factor in the simulation, while dashed lines do.